

Mathematical Modeling of Topical Drug Delivery in Women's Health

by

Daniel R. Adrianzen Alvarez

Department of Biomedical Engineering  
Duke University

Defense Date: October 27, 2023

Approved:

David F. Katz, Supervisor

George Truskey

Amanda Randles

Nimmi Ramanujam

Jim Smith

Dissertation submitted in partial fulfillment of  
the requirements for the degree of  
Doctor of Philosophy in the Department of  
Biomedical Engineering in the Graduate School  
of Duke University

2023

ABSTRACT

Mathematical Modeling of Topical Drug Delivery in Women's Health

by

Daniel R. Adrianzen Alvarez

Department of Biomedical Engineering  
Duke University

Defense Date: October 27, 2023

Approved:

David F. Katz, Supervisor

George Truskey

Amanda Randles

Nimmi Ramanujam

Jim Smith

An abstract of a dissertation submitted in partial fulfillment of the requirements for the degree of Doctor of Philosophy, in the Department of Biomedical Engineering in the Graduate School of Duke University

2023

Copyright by  
Daniel R. Adrianzen Alvarez  
2023

## Abstract

Our lab focuses on developing and optimizing drug delivery systems for applications in women's health. In this field, development of drugs and drug delivery systems is hindered by a heavy reliance on empirically derived data, usually obtained from non-standardized, highly variable *in vitro* and *in vivo* animal experiments. Further, without a mechanistic understanding of the various phenomena progressing during drug delivery, experiments tend to explore complex parameter spaces blindly and randomly. Deterministic mathematical models can improve the efficiency of this process by informing rational drug and product design. In this work, we were interested in two applications: 1. drug delivery of topically applied anti-HIV microbicides to the female reproductive tract; and 2. Localized intratumoral injections of ethanol-ethyl cellulose mixtures for treatment of cervical lesions.

Development of topically applied anti-HIV microbicides to prevent sexual HIV transmission is inefficient, with *in vitro* and *in vivo* tests having limited applicability to real product use. This issue is exacerbated by the dependence of drug performance on adherence and drug-administration conditions, which are not tested until clinical trials. Further, the lack of a standardized pharmacodynamic (PD) metric that is dependent on the heterogeneous dynamics of viral transport and infection makes it difficult to identify the most promising drug candidates. Here we develop a deterministic mathematical model that incorporates drug pharmacokinetics (PK) and viral transport and dynamics to estimate the probability of infection (POI) as a PD metric that can be computed for a variety of anti-HIV drugs in development. The model reveals key mechanistic insights into the spatiotemporally dependent dynamics of infection in the vaginal mucosa,

including susceptibility to infection at different phases in the menstrual cycle. Further, it and can be used as a platform to test novel drugs under several conditions, such as the timing of drug administration relative to the time of HIV exposure.

Localized injections of ablative agents, immunotherapeutics and chemotherapeutics have potential for increased therapeutic efficacy against tumors and reduced systemic effects. However, injection outcomes thus far have been largely unsatisfactory, due to unintended leakage of the active pharmaceutical ingredients (APIs) to non-target tissues. Adding a gelling or precipitating agent to the injection can help ameliorate this limitation, by acting to contain the API within the target tissue. One such example is injection of ethanol-ethyl cellulose mixtures. Due to the insolubility of ethyl cellulose in water, this polymer phase-separates in the aqueous tumor environment, forming a fibrous gel that helps contain ethanol, the current ablating agent (and chemotherapeutic drugs in the future), within the boundaries of the tumor. Our collaborators have shown that this strategy can be an effective low-cost treatment strategy for superficial solid tumors, with cervical cancer and cervical dysplasia, and liver cancer, being promising targets.

Here we present a mathematical model that enables characterization of the injection process. Our model uses Cahn Hilliard theory to model the phase separation of a precipitating or gelling agent during injection into poroelastic tissue. This theory is linked to the soft mechanics of tissue deformation during the injection, and to mass transport theory for the API. The model predicts key elements of the injection process, including the pressure field, the soft tissue displacement field, the phase constitution of the precipitating or gelling agent in the tissue, and the concentration distribution of the API in the tissue. The model enables us to explore relationships between these

elements and fundamental injection and tissue parameters. This can inform design of optimized injection protocols. Select model predictions include that larger injection volumes do not significantly affect cavity volumes but do lead to faster transport of the API to target tumor tissue. However, although higher flow rates lead to larger cavities – in the absence of tissue fracture, and when injected volume is held constant – they also lead to slower delivery of the API into the target tumor tissue. This is due to the shorter injection times. Importantly, concentration distributions of the API are not sensitive to the speeds of precipitation of the precipitating agents or to diffusion coefficients of the API in the dense (gelled) phase of the injectate material. The model presented here enables first-pass exploration of injection parameter space for select tissue types (properties). This can aid in optimization of localized therapeutic injections in a range of applications.

## **Dedication**

This dissertation is dedicated to Mrucha, who I know would have given anything to attend my defense.

Gracias por criarme de la manera que lo hiciste. Hoy soy un reflejo tuyo.

# Contents

Abstract.....	iv
List of Tables.....	xi
List of Figures.....	xii
1. Introduction .....	1
1.1 Background .....	1
2. Deterministic Mathematical Model Estimates the Probability of Sexual Transmission of HIV with and without Topical Administration of Anti-HIV Microbicides.....	6
2.1 Introduction .....	6
2.2 Methods .....	12
2.2.1 Geometry.....	12
2.2.2 Drug Transport and Diphosphorylation Kinetics in Vaginal Tissue .....	13
2.2.3 HIV Transport in Vaginal Tissue.....	14
2.2.4 TFV-DP Protection and Viral-Cell Dynamics in Tissue .....	15
2.2.5 Viral-Cell Dynamics and TFV-DP Protection in Blood.....	17
2.2.6 Boundary and Initial Conditions in Tissue .....	18
2.2.7 Parameter Choice and Exploration .....	20
2.2.8 Determination of Infection and POI Computation.....	25
2.2.9 Solving the Equations Numerically.....	26
2.2.10 Exploring Effects of TFV Administration and User Adherence on Infection .	26
2.2.11 Analyzing The Susceptibility To Infection At Different Stages In The Menstrual Cycle.....	28
2.3 Results and Discussion.....	29
2.3.1 Viral Load and Cell Densities Throughout Infection Process .....	29
2.3.2 Effect of Drug Administration on the POI .....	31

2.3.4 Susceptibility to Infection During the Luteal Phase and Follicular Phases of the Menstrual Cycle.....	34
2.3.6 Limitations of the Study .....	37
2.4 Conclusion .....	38
3. Modeling Phase-Transitioning Therapeutic Injections into Superficial Solid Tumors..	40
3.2 Introduction .....	41
3.2 Methods .....	45
3.2.1 Problem Definition .....	45
3.2.2 Biphasic Poroelastic Tissue Deformation.....	47
3.2.3. Phase Separation of the Gelling Agent .....	49
3.2.4 API Mass Transport.....	51
3.2.5 Parameter Choice .....	53
3.2.6 Obtaining Numerical Solution.....	55
3.3 Results and Discussion.....	56
3.3.1 Effect of Tissue Properties on Solid Deformation and Mass Transport.....	56
3.3.2 Effect of Injection Parameters on API Retention in Tumor Tissue .....	58
3.3.3 Precipitation Dynamics and Diffusion Coefficients have Small Effect on API Tumor Retention.....	60
3.3.4 Model Limitations .....	64
3.4 Conclusions.....	67
3.4.1 Application to Ethanol-Ethyl Cellulose Injections .....	68
3.4.2 Implications for Injections in Different Tissue Types .....	71
4. Conclusion and Future Directions .....	75
4.1 Future Directions .....	78
References.....	82

## List of Tables

Table 1: Parameters in the model that relate to the microbicide drug TFV and its active form TFV-DP.....	23
Table 2: Parameters in the model that relate to HIV virions. ....	23
Table 3: Parameters in the model that relate to the host environment and its interactions with HIV. ....	24
Table 4. Default parameters used in intratumoral injection model.....	55

## List of Figures

Figure 1: Geometry of model, including HIV (red), TFV (blue) and TFV-DP (green). .....	12
Figure 2: 3-compartment viral transport model comparison with experimental measurements.....	21
Figure 3: Representative log-normal distributions of simulation parameters used in Monte Carlo method, given $N = 100,000$ . .....	25
Figure 4: Representative viral loads and cell densities for 3 cases:.....	30
Figure 5: Distribution of drug molecules and efficacy throughout the domain. ....	32
Figure 6: Probability of Infection (POI) relative to different drug administration conditions at midcycle. ....	33
Figure 7: Probability of Infection (POI) during the follicular phase, luteal phase and at midcycle in the presence and absence of drug administration.....	35
Figure 8 Representative cartoon of injection process.....	43
Figure 9 Effect of varying hydraulic conductivity and tissue elasticity on cavity radius, and API mass transport .....	57
Figure 10 Effect of injection parameters $Q$ and $V$ on pressure, cavity radius, fluid velocity and on final distribution of API within domain. ....	59
Figure 11 Effect of mobility coefficient $M$ on gelling agent precipitation dynamics and resulting API mass transport.....	61
Figure 12 Effect of varying the diffusion coefficient in the dense phase of the gelling agent on API mass transport. ....	63

## Acknowledgements

First and foremost, I would like to thank my Ph.D. advisor Professor David Katz, who I met fortuitously during my M.S. when I applied to be a teaching assistant for his class. He has been incredibly supportive mentor since the day we first met. It was a joy having conversations with him not just about research and science, but also about football, South American politics, movies, wine, shoes... I feel incredibly privileged and thankful to have connected with him professionally and personally.

I would also like to thank each of my committee members. Professor George Truskey, who as my M.S. thesis advisor, was the determinant factor in my decision to jump into the beautiful abyss of computational work. Professor Amanda Randles, Professor Nimmi Ramanujam, and Dr. Jim Smith, thank you all for your guidance and wise suggestions throughout this journey. A special thanks to Jim, who took up so much of his time to discuss HIV modeling with me. I hope I didn't bore you too much with all the math!

A special thanks as well to current and past Katz lab members. Alan Sze, who gave extraordinarily valuable suggestions and who has always been a great friend. Yajing Gao, my predecessor, whose work was largely the basis for my own, Palm Chuchuen, for her incredible tutelage when I was dipping my toes into the turbid ocean of experimental work. Jenny Peters, Marcus Henderson and Mike Desoto, who kept the lab running for so long and were always so incredibly helpful. Mike, I miss you man!

I would also like to acknowledge our collaborators. Rob, Corrine, Erika, Jenna, Roujia, Katriana, thank you all. It was fun doing science with you.

Finally, I would like to thank the people most important to me. To my dad, a real-life superhero and eternal pillar of strength, and my sister Fiorella, the best sibling one could ask for. Your support keeps me sane and grounded. To my mom, your memory gives me strength. Lastly to my beautiful girlfriend Lindsay, who in the weeks running up to my defense, when I had been reduced to an empty carcass infested with disease and exhaustion, put me on her back and carried me to the promised land. I could not have finished this dissertation without you.

# 1. Introduction

## 1.1 *Background*

The process of drug development is lengthy, inefficient, and expensive due to its inherent reliance on empirically driven design. At the pre-clinical stage, drug candidates are tested through *in-vitro* assays and animal experiments to evaluate drug pharmacokinetics (PK) and pharmacodynamics (PD), which are subject to significant variability due to non-standardization of protocol methods and parameters used. The lack of standardization makes it difficult to compare candidate drugs and drug delivery formulations, resulting in a high rate of failure at the next step of the development pipeline [1].

Predictive mathematical modeling can speed up this process and make it more efficient by providing a means to obtain a deeper, mechanistic understanding of the various phenomena occurring simultaneously throughout drug delivery process. It may also allow comparisons between drugs and drug delivery formulations in a more even playing field. A good option for this purpose is deterministic, top-down modeling, which consists of leveraging foundational physical governing equations to model or fit experimental observations [2]. One such example is classical PK modeling, which uses mass conservation principles to characterize drug transport between compartments, using first order mass transport kinetics to model exchange between compartments [3]. However, these models usually assume instantaneous perfect mixing inside compartments and deal with volumetric averages, ignoring the nuances of spatiotemporal dynamics which is fundamental to so many transport processes. Further, they also usually rely on several black box parameters that are difficult to interpret physically or measure experimentally, making them prone to overfitting to a particular

dataset instead of having generalizable value. Our goal in this dissertation, was to develop powerful mathematical models of drug delivery systems that account for spatiotemporal heterogeneity, and that could be used to improve the efficiency of the drug development pipeline.

In the context of drug development for women's health, there were two drug delivery problems upon which we focused. The first was topical drug delivery of anti-HIV microbicides to the women's reproductive tract to protect against HIV infection. Although multiple preventative strategies exist such as oral and intravenous drug administration, cost and distribution, compounded by the need for consistent frequent intake, limits the accessibility of these solutions in the developing world [4]. Topically applied microbicides are an attractive alternative, providing women control over their anti-HIV protection and giving them the power to choose the microbicide product that best fits their preferences. However, development of these products suffers from the same issues of classical drug development, with many candidates showing promising results *in vitro*, but very modest efficacy in clinical trials [5]. This is partially due to improper administration and user adherence, which cannot be tested reliably in the pre-clinical stage.

To help address this issue, our goal was to develop a deterministic mathematical model that would enable standardized PKPD comparisons between different microbicide drugs and delivery methods. We were particularly interested in estimating the probability of HIV infection, as this is the ultimate metric of efficacious protection for any anti-HIV drug and could be used easily as a standardized benchmark. The model presented in this work tackles this problem. The infection process is rich in complexity, with drug molecules, HIV virions and cells interacting across space and time, and these various interactions affecting the outcome of infection. By tracking viral transport, drug transport

and viral dynamics in vaginal mucosal tissue (where infection can occur) with spatiotemporal detail, our model enables analysis of the probability of infection under different drug dosing conditions. Further, using the Monte Carlo method, we were able to account for variations in viral infection parameters and anatomical variations between individuals. This gave opportunities to analyze the infection process more deeply, for example, gaining insights about the susceptibility to HIV infection at different stages of the menstrual cycle. For our analysis, we focused on the drug Tenofovir (TFV), applied topically via an intravaginal gel. This is a widely used drug in HIV pre-exposure prophylaxis (PrEP) and therapy for HIV infections [6-8]. However, in theory the model should be extendable to any topically applied drug if we have knowledge on that drug's transport properties and dose-response characteristics. In future studies, more rigorous testing must be done on this model to gauge its versatility and ability to compare different topical drug delivery systems, for example, intravaginal rings and dissolving inserts, under various infection and drug administration conditions [9].

The second project was centered around low-cost treatment of cervical dysplasia and cancer. Work by our collaborators showed that intratumoral injections of ethanol-ethyl cellulose mixtures could function as an alternative to surgery for solid tumors in initial animal models [10, 11]. Ethyl cellulose is insoluble in water; therefore, it phase-separates in the aqueous tumor environment and forms a thick precipitate similar to a gel. This helps to contain ethanol within the boundaries of the tumor [10]. Application of this strategy to the cervix was particularly attractive due to the superficial nature of cervical tumors, and the potential for a low-cost alternative to expensive surgeries or other excisional procedures in low- and middle-income countries, where cervical cancer continues to be the second highest cause of cancer-related death in women [12].

Experimental work has been instrumental in providing insights into the dependence of drug PK upon injection parameters [10-15]. However, these experiments reveal only snapshots into the dynamics of the injection process and do not give a complete picture of the complex dependence of drug PK to injection parameters and tissue-specific parameters. Predictions via mathematical modeling could provide a valuable solution to speed up optimization of this drug delivery system for several tissue types.

Prior injection models have effectively characterized poroelastic tissue deformation and mass transport during an injection [16-18], but to our knowledge, there is no mathematical model that couples these theories to phase separation of a co-injected substance like ethyl cellulose, that reduces the rate of transport and keeps ethanol within the tumor. In this work, we present a model that tackles this issue, by coupling together biphasic poroelastic tissue deformation, Cahn-Hilliard phase-separation theory and mass transport in a single mathematical framework. We kept our initial model general, to keep it as simple and generalizable to injection of multiple tumor ablative agents and gelling or phase-separating agents. Testing of the model revealed interesting insights about drug PK, including for example varying drug retention for injections in tumor tissues with different stiffnesses. Further, the model also predicted relationships between drug PK and the dynamics of phase separation. In the future, the model needs to be tuned more specifically to fit the ethanol-ethyl cellulose injection application for treatment of cervical cancer. This includes comparing predicted outputs including pressure (a primary causative factor for tissue rupture), the distribution of the phase separated ethyl cellulose, and ethanol concentration profiles to experimental results. These could begin with simplified experimental measurements of injections in various surrogate materials for model testing and parameter estimation. A key part of

establishing the link between the model and injection experiments of ethanol-ethyl cellulose is determining the relationship between ethyl cellulose concentration in the initial mixture and viscosity, rate of phase separation, and the diffusion coefficient of the drug within the solidified ethyl cellulose. Although outside of the scope of this dissertation, ultimately, our goal is to use this model to inform design of better intratumoral injections, focusing on cervical tumors but expanding to other tissue types as well.

In this work, through the lens of these two projects, we have examined the value and applicability of deterministic mathematical models to important drug delivery problems in women's health. Given the findings obtained, we propose that future deterministic math modeling be incorporated into the drug development pipeline to reduce inefficiencies and accelerate the rate of novel drug development.

## **2. Deterministic Mathematical Model Estimates the Probability of Sexual Transmission of HIV with and without Topical Administration of Anti-HIV Microbicides**

### **2.1 Introduction**

Efforts to develop novel anti-HIV drugs have led to multiple preventative strategies including oral, intravenous and subcutaneous administration of pre-exposure prophylactic (PrEP) drugs [19, 20]. However, the accessibility of these products in the developing world is hindered by cost, storage, and distribution limitations. These issues are exacerbated by the strict dosing requirements of oral PrEP, the lead preventative modality, which usually consist of daily intake. Topically delivered microbicides to the vaginal tract may provide a valuable alternative to bypass some of these hurdles. Topical intravaginal delivery vehicles include gels, dissolving tablets, and films, which can be applied on-demand to deliver anti-HIV drugs prior to sexual exposure, and intravaginal rings (IVRs), which offer sustained-release for extended protection. For example, Dapivirine-releasing IVRs slowly release the anti-HIV drug Dapivirine into the vaginal environment over the span of 28 days, reducing the incidence of HIV infection by 27 to 37% relative to placebo [21, 22]. This ring was approved for use in many countries in 2020 (but not in the U.S.) and is currently distributed and used in Eastern and Southern Africa [23]. Development of a range of effective topically administered microbicide products is needed to improve accessibility to preventative HIV care, cater to different user preferences, and reduce the likelihood of improper user adherence.

The standard product development process for novel microbicides focuses on efficacy testing of potential drug candidates through intensive and costly pre-clinical *in vitro* and *in vivo* experiments. These experiments are not standardized, so protocols

used for development and testing of one microbicide may differ substantially from protocols used on other anti-HIV drugs. This experimental variability makes it difficult to compare between drugs formulations and delivery vehicles, posing a significant barrier to the development of efficacious anti-HIV microbicides [24]. Further, at this stage it is difficult to preemptively gauge the impact of inter-user variability and heterogeneity on drug efficacy, particularly due to variations in drug administration. Indeed, several innovative anti-HIV products have exhibited significant protective efficacy *in vitro* and *in vivo* during animal testing [25], but their efficacies at the point-of-care and throughout clinical trials have been modest or even negative [26], often due to inconsistent, and at times, inadequate consumer adherence [27]. A tool that enables these types of analyses would greatly facilitate the design and development of products that are both efficacious and have a high “forgiveness” tolerance to inadequate user administration and natural inter-user variability.

Computational models of drug delivery provide a unique platform to facilitate microbicide product optimization rapidly and inexpensively prior to clinical trials. Further, they can predict drug pharmacokinetics (PK) *in vivo* with a greater degree of accuracy than ex-vivo measurements on biopsies, which have been shown to overestimate drug concentrations in the vaginal stroma by as much as one order of magnitude [28]. Multicompartmental pharmacokinetic (PK) models are particularly useful in providing initial insights into drug delivery, as they enable predictive computations of drug concentrations in different anatomical compartments. The most common and widely used modeling approach assumes homogenous drug distributions within compartments and first order drug transport exchanges between compartments [3]. However, such models only compute mass-averaged drug tissue concentrations and fail to capture the

spatial and temporal dependence of the physiochemical mechanisms that govern drug transport, including convection and diffusion. During acute sexual transmission of HIV, the heterogeneity imparted by these mechanisms is exacerbated by the native anisotropic features of vaginal tissue. Accounting for the spatiotemporal complexity of these processes and phenomena is key to making accurate predictions of drug PK in the female reproductive tract, where the physiology of the epithelial barrier and stroma affect the kinetics of drug transport and lead to exceedingly heterogeneous drug distributions [28-30]. Such heterogeneity confounds our understanding and interpretation of transport and infection created by sexually transmitted virions.

Our group has previously developed PK models that use deterministic mass conservation principles to track microbicide transport in the vaginal canal and mucosa with spatiotemporal detail, thereby accounting for spatial and temporal heterogeneity of the host environment [28-30]. Our initial models primarily analyzed Tenofovir (TFV), a broadly used anti-HIV drug that functions as a nucleoside reverse transcriptase inhibitor when phosphorylated in cells into Tenofovir Diphosphate (TFV-DP) [31, 32]. Our predicted TFV and TFV-DP PK aligned well with experimental PK studies [33]. We also established an initial link to pharmacodynamics (PD) by using a metric called Percent-Protected (PP), which captures the percentage volume of tissue that has drug concentrations greater than a specified  $EC_{50}$  or  $IC_{50}$ . This strategy provides first-pass insights into protection as a function of time, but it relies on a binary metric that does not fully capture the continuum between anti-HIV protection and microbicide concentration. Further, this metric does not account for viral kinetics and transport, which are central to the infection process during sexual HIV transmission.

Deterministic “viral-dynamics” mathematical models have been developed to quantitatively examine primary systemic HIV infection and capture the primary interactions between HIV and “infectible” CD4+ T-cells. Such models have exhibited remarkable accuracy in blood viral load predictions [34] and have enabled simplified predictions of complex processes including viral latency within infected cells [35, 36]. These models are valuable because they provide detail into acute infection and its progression, filling in the gaps left by experimental measurements that have limited sampling frequencies and give only snapshots into these processes. They are also useful at providing a mechanistic understanding of viral infection dynamics, thus facilitating interpretation of experimental observations [37, 38], providing a basis for design of new antiviral therapies and informing more effective clinical trials [39]. There have also been efforts to utilize the systemic models of HIV infection to propose a standardized, quantitative PD metric that evaluates anti-HIV protection: the Probability of Infection (POI) [40, 41]. This metric could facilitate efficacy comparisons between different microbicide products. However, these models have two distinct limitations. First, they assume homogenous distributions of infectible cells and HIV virions within a single compartment, which is a poor assumption for male-to-female sexual transmission in the female reproductive tract. In this scenario, it is vital to account for the heterogenous physiology of the vaginal canal because the presence of the epithelial barrier, coupled to the spatiotemporal mechanisms of drug transport, greatly influences the distribution of HIV virions, drug molecules and CD4+ infectible cell throughout tissue. This, consequently, affects virus-cell infection dynamics. Second, viral dynamics simulations use black box “efficacy” parameters to account for microbicide efficacy, which have no direct deterministic link to drug kinetics or spatiotemporal transport [42].

Here, we developed a deterministic multicompartmental model that couples deterministic drug PK, spatiotemporal HIV transport, and drug-cell and HIV virion-cell kinetics into a single modeling framework that characterizes male-to-female sexual HIV transmission. The resulting system of coupled partial and ordinary differential equations deterministically characterize the instantaneous spatiotemporal heterogeneity of target cells, infected cells, virions, and drug molecules across various depths in the vaginal canal, including the lumen, epithelium, and stroma. The model accounts for exchange and transport to a blood compartment where analogous drug-cell and virion-cell dynamics also occur, enabling computation of average blood concentrations of cells, HIV, and drug. The predicted viral load in the blood is examined to determine if infection has occurred given specific parameter combinations. Ultimately, the model presented allows us to predict the outcome of sexual HIV exposure as a function of anatomical, physicochemical, and dosing parameters.

Our analysis focused on topical delivery of TFV via an intravaginal gel, and its activation to TFV-DP in cells. TFV is an appropriate drug to choose as a starting point due to the vast amount of data available on its PK characteristics, dose-response profile, and clinical efficacy, which facilitates parameter estimation and model evaluation [43-47]. However, the mathematical framework presented here can be readily extended to a wide array of topically applied anti-HIV microbicides, enabling quantitative comparisons between different drugs and delivery vehicles.

To account for user heterogeneity and enable a deeper exploration of PD, we generated lognormal distributions that capture the variability of various host and infection parameters, including epithelial thickness, the viral load in semen, viral clearance rates in the stroma and blood, initial infectible CD4+ T cell densities in blood and vaginal

tissue, and the production rate of new virions from infected cells. Then, we ran Monte Carlo simulations by sampling randomly from these distributions to simulate a population of different women exposed to sexual HIV transmission. By identifying the number of positive infections in this population, we computed the POI and investigated its use as a standardized PD metric for topical microbicide administration under a range of circumstances. We were particularly interested in using the model to explore two focus points: 1. the impact of drug administration adherence on efficacy and 2. infection susceptibility in relation to the menstrual cycle. For focus 1, we studied the influence of user adherence on the POI by varying the time delay between drug administration and viral exposure. This study revealed insights into the ‘forgiveness’ of TFV to improper use, either due to early administration, up to 4 hours before exposure, or due administration post-exposure instead of on-demand application as intended for a TFV gel. To evaluate the POI due to exposure at different stages of the menstrual cycle, as per focus 2, we adjusted the target cell density in vaginal tissue and the epithelial thickness as observed experimentally, with a higher CD4+ T cell density [48-50] and a thinner epithelium [49] during the luteal phase as compared to the follicular phase. Results of this analysis emphasize the sensitivity of the infection outcome on the density of CD4+ T cells in the vaginal submucosa, agreeing with studies that indicate an increase in susceptibility to HIV infection when there is inflammation in the vaginal tract [43, 51].

Ultimately, the mechanistic model presented here couples viral transport, drug transport and activation kinetics, and viral-cell dynamics, to characterize HIV infection in the female reproductive tract and its prevention due to topical administration of a TFV gel. By incorporating spatiotemporal detail to our analysis in the vaginal tract, including

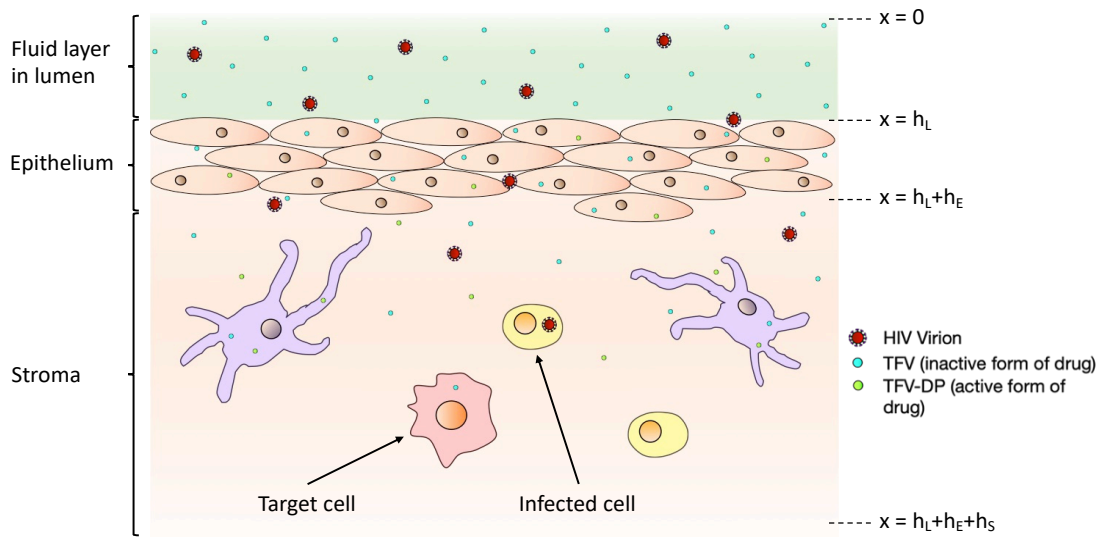


**Figure 1: Geometry of model, including HIV (red), TFV (blue) and TFV-DP (green).**

Here we assume one-dimensional top-down diffusion from the lumen, through the epithelium and into the stroma, where we assume homogenously distributed target, infectible immune cells.

transport to the blood, and accounting for population-wide inter-user variability, the model enables detailed and nuanced exploration of PD as a function of the host environment and details of host microbicide administration.

## 2.2 Methods

### 2.2.1 Geometry

We modeled one-dimensional, transversal transport of HIV virions and drug molecules through three compartments in the vaginal canal: the lumen, the epithelium, and the stroma (Figure 1). We set the thickness of the lumen to 800 $\mu$ m, assuming a homogenously distributed microbicide volume of 4mL ( $h_L = 400\mu$ m), and a net epithelial surface area of 100cm<sup>2</sup> [28]. We also assumed rectilinear, top-to-bottom symmetry about the centerline of the lumen, which we defined as the origin ( $x = 0$ ). The epithelium consists of a layer of tightly packed cells, forming a stratified squamous layer [52]. Here, we

assumed that this layer had a uniform thickness  $h_E$  throughout the length of the canal.  $h_E$  was one of the patient-specific parameters that defined a characteristic of our “simulated patient population”, described in section D. The stroma lies below the epithelium and contains CD4+ T cells (i.e. target cells), which are susceptible to infection upon collisions with HIV virions. For simplicity, we assumed that these cells are homogenously distributed within a stromal layer of thickness  $h_S$ .

Importantly, we assume that in the lumen, the TFV gel fills the entire width of the vaginal canal. When seminal deposition containing virions occurs, the viral load and initial concentration of drug is halved following a 1:1 dilution ratio. We also assume that this 1:1 dilution ratio holds irrespective of the relative timing of drug administration and HIV exposure.

### 2.2.2 Drug Transport and Diphosphorylation Kinetics in Vaginal Tissue

TFV transport through tissue is governed by a coupled system of unsteady mass-transport diffusion equations, following Fick’s Second Law through the lumen, epithelium and stroma, characterized by equations 1-3 respectively [28]. In the absence of drug, deposited semen fills the entirety of the lumen during HIV exposure. When the TFV gel is administered, we assume the lumen gets filled by a homogenous mixture of semen and gel.

$$\frac{\partial C_{TFV,L}}{\partial t} = D_{TFV,L} \frac{\partial^2 C_{TFV,L}}{\partial x^2} - k_{TFV,D} C_{TFV,L} \quad (1)$$

$$\frac{\partial C_{TFV,E}}{\partial t} = D_{TFV,E} \frac{\partial^2 C_{TFV,E}}{\partial x^2} - \frac{dC_{DP,E}}{dt} \quad (2)$$

$$\frac{\partial C_{TFV,S}}{\partial t} = D_{TFV,S} \frac{\partial^2 C_{TFV,S}}{\partial x^2} - k_{TFV,B} C_{TFV,S} - \frac{dC_{DP,S}}{dt} \quad (3)$$

$$\frac{dC_{DP,i}}{dt} = K_{on} \left\{ C_{TFV} \varphi_i - \frac{C_{DP,i}}{r} \right\} - K_{off} C_{DP,i} \quad (4)$$

Here,  $C_{TFV}$  represents the concentration of TFV,  $D_{TFV,i}$  is the diffusion coefficient of TFV molecules in the anatomical compartment  $i$  (i.e. L – lumen, E-epithelium, and S – stroma). Additional loss terms are added in the lumen to account for dilution due to ambient vaginal fluid secretion and leakage out of the lumen, and in the stroma, to account for drug transport to the vasculature and lymphatics. These loss terms are modeled as first-order processes, with rate constants  $k_{TFV,D}$  and  $k_{TFV,B}$  respectively. TFV is phosphorylated in cells in the epithelium and stroma to its active component TFV-DP. We model TFV-DP production using  $K_{on}$  and  $K_{off}$  rate kinetics (equation 4), where production occurs at a rate that saturates based on the relative difference between the local TFV concentration in cells (given a compartmental cell volume fraction of  $\varphi_i$  in compartment  $i$ ) and the local concentration of TFV-DP ( $C_{DP}$ ), normalized by the fraction  $r$  of TFV that can be dephosphorylated [29]. Similarly, we assume that conversion back to TFV also occurs, but at a much slower rate  $K_{off}$ . This process occurs in both the epithelium and stroma.

### 2.2.3 HIV Transport in Vaginal Tissue

Movement of HIV virions in fluids has been characterized as a diffusive process [53, 54]. In vaginal epithelium, studies suggest that transport also occurs in a diffusion-like manner [55, 56]. This allows us to assume that throughout all three compartments,

HIV transport is governed by Fick's Second Law of diffusion. Thus, we developed a system of coupled partial differential equations governing this phenomenon in the lumen, epithelium, and stroma (equations 5-7).

$$\frac{\partial C_{V,L}}{\partial t} = D_{V,L} \frac{\partial^2 C_{V,L}}{\partial x^2} - k_{V,D} C_{V,L} \quad (5)$$

$$\frac{\partial C_{V,E}}{\partial t} = D_{V,E} \frac{\partial^2 C_{V,E}}{\partial x^2} \quad (6)$$

$$\frac{\partial C_{V,S}}{\partial t} = D_{V,S} \frac{\partial^2 C_{V,S}}{\partial x^2} - k_{V,B} C_{V,S} + \rho C_{I,S} \quad (7)$$

The model is analogous to that of TFV transport in all three compartments, allowing us to track the local number density of HIV,  $C_V$ , in all three compartments L, E and S. However, in the stroma there is also an additional term that accounts for the production of new virions (V) from infected cells (I) at a rate  $\rho$ , which establishes a link between viral transport and viral dynamics.

#### 2.2.4 TFV-DP Protection and Viral-Cell Dynamics in Tissue

One of our objectives for the model was to have a metric of drug efficacy that was a continuous function of the local concentration of drug, allowing us to form a direct, continuous link between PK and PD. To this end, we used an empirically derived expression for the dose-response of TFV-DP (equation 8). Variations of this equation can be utilized to match different classes of anti-HIV drugs, such as other reverse transcriptase inhibitors (NRTIs), non-nucleoside reverse transcriptase inhibitors

(NNRTIs), protease inhibitors (PIs), etc. The output to this equation is the drug efficacy  $q$ , which is bound between 0 and 1, corresponding to negligible efficacy to perfect efficacy. In tissue,  $q$  depends on  $x$  and  $t$  because the concentration of TFV-DP depends on  $x$  and  $t$ .

Models of viral dynamics use mass conservation to compute densities of virus and cells, including healthy target cells  $T$  and infected cells  $I$ . These models commonly simplify the interactions between virions and cells into a first order infection term that is proportional to  $C_V$  and  $C_T$  and has a constant of proportionality  $\beta$  which represents viral infectivity [34]. Similarly, cell-to-cell infection is also represented as a first order term, in this case proportional to  $C_T$  and  $C_I$ , with the constant of proportionality being the cell-to-cell infection rate  $\omega$ .  $C_T$  and  $C_I$  also include a loss term due to cell death given by rates  $d_T$  and  $d_I$ , and  $C_T$  also has a natural production rate  $\lambda$ . Here, we implement this mathematical formulation (equations 9 and 10), but we also include a diffusion term to account for cell movement which adds a dependence on  $x$ , thereby making these partial differential equations that capture heterogenous cell densities in tissue.

As a NRTI, here we assume that TFV-DP hinders the ability of free virions to successfully infect cells but it does not block cell-to-cell infection or affect the production rate of new virions from infected cells, fitting experimental observations [57, 58]. Following this logic, drug efficacy  $q$  reduces the rate of free virion-to-cell infection in equations 9 and 10. When  $q$  is 1, the infection term drops to 0, resulting in perfect protection from free virion-to-cell infection. However, cell-to-cell infection may still occur as it remains unaffected by TFV-DP. The drug efficacy  $q$  can be applied to different terms in these equations to match the mechanism of action of different classes of drug.

$$q(C_{DP}) = \frac{1}{1 + \frac{IC_{50}}{C_{DP}}} \quad (8)$$

$$\frac{\partial C_{T,S}}{\partial t} = D_{T,S} \frac{\partial^2 C_{T,S}}{\partial x^2} + \lambda - d_T C_T - (1 - q) \beta C_V C_T - \omega C_I C_T \quad (9)$$

$$\frac{\partial C_I}{\partial t} = D_{I,S} \frac{\partial^2 C_I}{\partial x^2} + (1 - q) \beta C_V C_T + \omega C_I C_T - d_I C_I \quad (10)$$

### 2.2.5 Viral-Cell Dynamics and TFV-DP Protection in Blood

In the blood, we assume perfect mixing of all agents (i.e. virus, drug, cells), such that the concentrations are homogenous throughout the entire volume. This converts the mass balance equations to ordinary differential equations that depend only on time, matching most models of Viral Dynamics. Transport of drug and virus from the tissue to the blood is computed via a mass transport rate that is given by the volumetric integral of the loss term of agent  $j$  (i.e.  $j = \text{TFV}$  or  $j = \text{V}$ ) from the stroma to the vasculature (equation 11). This mass transport rate is an input to the mass balance equations in the blood. We track the concentration of TFV in the bloodstream by adding the mass influx rate of TFV normalized by the volume of distribution of TFV in the body, and then subtract out the loss term (modulated by rate  $k_{TFV,L}$ ) and the rate of conversion to TFV-DP (equation 12). The phosphorylation of TFV to TFV-DP given by constitutive equation 13 is analogous to equation 4 for phosphorylation in tissue.

The concentration of virus in the blood consists of a positive mass transport rate from the stroma normalized by the blood volume  $V_B$ , a loss term that progresses at a fixed rate  $k_{V,L}$ , and the production of new virions from infected cells modulated by  $\rho$

(equation 14). Finally, the cell densities in the blood (equations 15 and 16) mirror the equations in tissue (equations 9, 10), but exclude the diffusive transport term.

$$\dot{M}_{j,SB}(t) = 2WL \int_0^{h_S} k_{j,B} C_S dx \quad (11)$$

$$\frac{dC_{TFV,B}}{dt} = \frac{\dot{M}_{TFV,SB}(t)}{V_{TFV,B}} - k_{TFV,L} C_{V,B} - \frac{dC_{DP,B}}{dt} \quad (12)$$

$$\frac{dC_{DP,B}}{dt} = K_{on} \left\{ C_{TFV,B} \varphi_B - \frac{C_{DP,B}}{r} \right\} - K_{off} C_{DP,B} \quad (13)$$

$$\frac{dC_{V,B}}{dt} = \frac{\dot{M}_{V,SB}(t)}{V_B} + \rho C_{I,B} - k_{V,L} C_{V,B} \quad (14)$$

$$\frac{dC_{T,B}}{dt} = \lambda - d_T C_T - (1 - q) \beta C_V C_T - \omega C_I C_T \quad (15)$$

$$\frac{dC_{I,B}}{dt} = (1 - q) \beta C_V C_T + \omega C_I C_T - d_I C_I \quad (16)$$

## 2.2.6 Boundary and Initial Conditions in Tissue

At  $x = 0$  and  $x = h_L + h_E + h_S$ , we assume a no flux boundary condition for both HIV and drug transport (equations 17, 18). At the interface of the different compartments, (lumen-epithelium, epithelium-stroma), we apply a partition coefficient to account for different permeabilities (equations 19-22) and assume that the flux is scaled by the respective diffusion coefficients in each compartment (equations 23-26).

The initial conditions depend on the relative timing between drug administration and viral load exposure. If no drug is applied, the initial concentration of virus in the lumen is  $V_0$ . However, if drug was administered prior to exposure, this value is halved to reflect a 1:1 dilution. The same reasoning is applied to the initial drug concentration; it is  $C_0$  if exposure to HIV hasn't occurred yet and halved to reflect a 1:1 dilution if administered post-exposure. The initial condition for infectible target cells is  $T_{0,S}$ , in the stroma,  $T_{0,B}$  in blood and 0 everywhere else. Infected cells are initially 0 everywhere.

$$\frac{dC_{TFV}}{dx} = 0 @ (x = 0, h_L + h_E + h_S) \quad (17)$$

$$\frac{dC_V}{dx} = 0 @ (x = 0, h_L + h_E + h_S) \quad (18)$$

$$C_{TFV,E} = \phi_{TFV,LE} C_{TFV,L} @ (x = h_L) \quad (19)$$

$$C_{TFV,S} = \phi_{TFV,ES} C_{TFV,E} @ (x = h_L + h_S) \quad (20)$$

$$C_{V,E} = \phi_{V,LE} C_{V,L} \quad (21)$$

$$C_{V,S} = \phi_{V,ES} C_{V,E} \quad (22)$$

$$D_{TFV,E} \frac{dC_{TFV,E}}{dx} = D_{TFV,L} \frac{dC_{TFV,L}}{dx}, @ (x = h_L) \quad (23)$$

$$D_{TFV,S} \frac{dC_{TFV,S}}{dx} = D_{TFV,E} \frac{dC_{TFV,E}}{dx}, @ (x = h_L + h_S) \quad (24)$$

$$D_{V,E} \frac{dC_{V,E}}{dx} = D_{V,L} \frac{dC_{V,L}}{dx}, @ (x = h_L) \quad (25)$$

$$D_{V,S} \frac{dC_{V,S}}{dx} = D_{V,E} \frac{dC_{V,E}}{dx}, @ (x = h_L + h_E) \quad (26)$$

$$C_{TFV}(x, 0) = \begin{cases} C_0, & x \leq h_L \\ 0, & x > h_L \end{cases} \quad (27)$$

$$C_V(x, 0) = \begin{cases} V_0, & x \leq h_L \\ 0, & x > h_L \end{cases} \quad (28)$$

$$C_T(x, 0) = \begin{cases} 0, & x \leq h_L + h_E \\ T_{0,S}, & x > h_L + h_E \end{cases} \quad (29)$$

## 2.2.7 Parameter Choice and Exploration

Parameters were either references from prior studies, estimated or fit from experimental observations in the literature or varied to explore their impact on the results. Tables 1-3 specify the values for these parameters and their sources.

A key component of our analysis is the ability to estimate the POI, which requires running our model for different parameter ranges to simulate different host environments, HIV exposure conditions and drug administration conditions. The parameters in the tables that contain a standard deviation, namely  $h_E$ ,  $k_{B,V}$ ,  $k_{L,V}$ ,  $V_0$ ,  $\beta$ ,  $T_{0,B}$ ,  $T_{0,S}$  were part of our Monte Carlo simulations used to estimate the POI. They were chosen because they are fundamental to the dynamics of infection and because they have high natural variability, thus allowing us to account for the intrinsic variation

amongst different hosts and infection conditions. We created log-normal distributions using the means and standard deviations provided for these parameters and sampled from them randomly to obtain suitable parameter combinations. Log-normal distributions were chosen because the standard deviation of these parameters is so high that the left tail of normal distributions delve well into the negatives. Lognormal distributions are skewed to have shorter left tails, thus reducing the likelihood of negative parameters. Further, lognormal distributions are seen frequently in biological processes, making them a good fit for our problem [59-61]. To eliminate the risk of negative or unreasonably small values of the parameters, we also truncated the distributions at negligible values close to 0.

The diffusion coefficient of the virus in epithelium  $D_{V,E}$ , the loss rate of the virus in the lumen  $k_{D,V}$  and the partition coefficient  $\phi_{V,LE}$  were estimated by creating a simplified viral transport model. This model consisted of equations 5-7, excluding the  $\rho$  term that accounts for production of new virions from infected cells. Using these equations, we

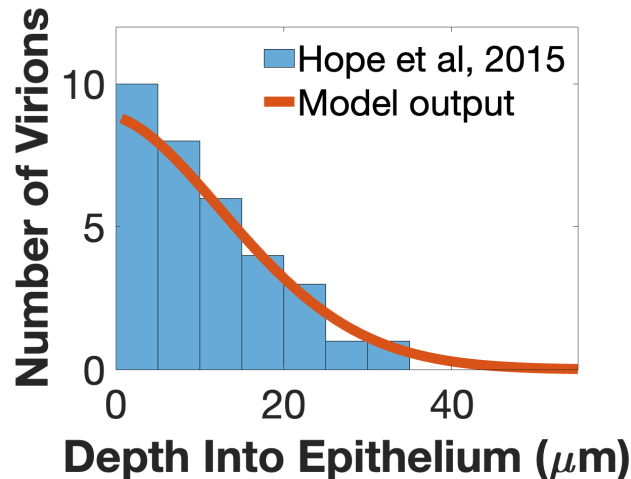


**Figure 2: 3-compartment viral transport model comparison with experimental measurements.**

predicted the number of virions in space and time and fitted our results to reported experimental measurements by Carias et al. of the viral distribution in vaginal epithelium 4 hours post-inoculation [55]. The results of this fit are shown in Figure 2. In this model, we also assumed that  $D_{V,S}$  was an order of magnitude larger than  $D_{V,E}$ , given the cell volume fraction differences between the epithelium and stroma. However, we kept a value of unity for the partition coefficient between the epithelium and stroma  $\phi_{TFV,ES}$  for simplicity, and because we did not expect any significant viral density step drop between the epithelium and the stroma but rather just the continuous drop resulting from diffusive transport.

$\beta$  and  $\omega$  are complex to estimate. Previous reports of these values obtained estimates by using viral dynamics models and fitting their computations of the viral load in the blood to clinically measured data in infected humans [34], and so we surmise that this is likely an overestimation. In our model, we want to use values of  $\beta$  and  $\omega$  that are more fitting with a balanced population of at-risk women who may or may not get infected after exposure. We reduced the values of these parameters to a lower range arbitrarily, while keeping the ratio between them approximately the same. Fitting our predictions of the POI may be necessary for a more accurate assessment of the value of these parameters.

The volume of vaginal fluid in the lumen was varied depending on the phase of the menstrual cycle, with 0.25mL, 0.5mL and 1mL for the luteal phase, follicular phase, and at midcycle respectively. Given these values, the thickness of the lumen  $h_L$  was estimated by dividing the total volume of fluid in the lumen at any given time (i.e. the volume of vaginal fluid  $V_f$ , the volume of semen  $V_s$  and the gel volume  $V_g$ ) by the surface area of the lumen  $SA$ .

**Table 1: Parameters in the model that relate to the microbicide drug TFV and its active form TFV-DP.**

Symbol	Description	Value	Source
$C_0$	Initial drug concentration in the lumen	$10^7$ ng/mL	[62]
$V_g$	Volume of gel	2mL	[28]
$D_{TFV,L}$	Diffusion coefficient of TFV in the lumen	$6 \times 10^{-6}$ cm <sup>2</sup> /s	[28]
$D_{TFV,E}$	Diffusion coefficient of TFV in the epithelium	$7 \times 10^{-8}$ cm <sup>2</sup> /s	[28]
$D_{TFV,S}$	Diffusion coefficient of TFV in the stroma	$4 \times 10^{-7}$ cm <sup>2</sup> /s	[28]
$\phi_{TFV,LE}$	TFV partition coefficient at the lumen/epithelium interface	0.75	[28]
$\phi_{TFV,ES}$	TFV partition coefficient at the epithelium/stroma interface	1	[28]
$k_{TFV,D}$	TFV loss rate constant in the lumen due to dilution	1.22 hr <sup>-1</sup>	[28]
$k_{TFV,B}$	TFV loss rate from the stroma to blood / lymphatics	0.119 hr <sup>-1</sup>	[28]
$k_{TFV,L}$	TFV loss rate in blood	1.41 hr <sup>-1</sup>	[28]
$K_{on}$	Rate of formation of TFV-DP	0.693 hr <sup>-1</sup>	[29]
$K_{off}$	Rate of elimination of TFV-DP	0.693 week <sup>-1</sup>	[29]
$r$	Fraction of TFV-DP converted from TFV	0.1	[29]
$V_{TFV,B}$	Volume of distribution of TFV	$7.5 \times 10^5$	[29]
$\tau_{VD}$	Timing between drug administration and HIV exposure.	-2,0,2 hrs	Varied

**Table 2: Parameters in the model that relate to HIV virions.**

Symbol	Description	Value	Source
$V_0$	Initial viral load in the lumen	$1 \times 10^4$ (s.d. $1 \times 10^5$ ) virs/mL	[63]
$V_s$	Volume of semen	2mL	[64]
$D_{V,L}$	Diffusion coefficient of HIV in the lumen	$1.3 \times 10^{-8}$ cm <sup>2</sup> /s	[53, 54]
$D_{V,E}$	Diffusion coefficient of HIV in the epithelium	$1 \times 10^{-10}$ cm <sup>2</sup> /s	Estimated
$D_{V,S}$	Diffusion coefficient of HIV in the stroma	$1 \times 10^{-9}$ cm <sup>2</sup> /s	Estimated

$\phi_{V,LE}$	HIV partition coefficient in lumen/epithelium interface	0.75	Estimated
$\phi_{V,ES}$	HIV partition coefficient in epithelium/stroma interface	1	Estimated
$k_{V,D}$	HIV loss rate constant in the lumen due to dilution	0.3 day <sup>-1</sup>	Estimated
$k_{V,B}$	HIV rate of transfer from stroma to blood	5 (s.d. 5) day <sup>-1</sup>	Estimated
$k_{V,L}$	HIV loss rate constant in the blood	40 (s.d. 20) day <sup>-1</sup>	[34]
$\beta$	Viral infectivity	1x10 <sup>-7</sup> (s.d. 2.15x10 <sup>-7</sup> ) cm <sup>3</sup> virs <sup>-1</sup> day <sup>-1</sup>	Estimated

**Table 3: Parameters in the model that relate to the host environment and its interactions with HIV.**

Symbol	Description	Value	Source
$T_{0,S}$	Initial density of CD4+ target cells in the stroma	1x10 <sup>3</sup> cells/mL	[48, 65]
$T_{0,B}$	Initial density of CD4+ target cells in the blood	5x10 <sup>3</sup> cells/mL	[66]
$r_T$	Average radius of target cells	10 $\mu$ m	[67]
$SA$	Surface area of vaginal lumen in humans	100cm <sup>2</sup>	[29]
$V_f$	Average volume of vaginal fluid in the lumen	0.25, 0.5, 1 mL	Varied
$h_L$	Thickness of lumen	-	Estimated
$h_E$	Thickness of epithelium	200 (s.d. 78) $\mu$ m	[68]
$h_S$	Thickness of stroma	0.28 cm	[68]
$\varphi_E$	Volume fraction of cells in epithelium	0.95	[29]
$\varphi_S$	Volume fraction of cells in stroma	0.1	[29]
$\varphi_B$	Volume fraction of cells in blood (excluding RBCs)	0.01	[67]
$\lambda$	Average production rate of target cells	$d_T T_{0,i}$	[34]
$d_T$	Average death rate of target cells	0.01 day <sup>-1</sup>	[34]
$d_I$	Average death rate of productive infected cells	0.39 day <sup>-1</sup>	[34]
$\omega$	Rate of cell-to-cell infection	1.5x10 <sup>-4</sup> cm <sup>3</sup> cells <sup>-1</sup> day <sup>-1</sup>	Estimated
$\rho$	Average production rate of HIV from infected cells	850 virs hr <sup>-1</sup> (s.d. 1x10 <sup>3</sup> )	[34]

## 2.2.8 Determination of Infection and POI Computation

For our computations of the POI, we sampled randomly from the log-normal distributions described previously and ran 100,000 simulations (Figure 3). This simulated a population of 100,000 women with different host environments and infection circumstances. For each parameter combination, we computed the viral load in blood 18 days after HIV exposure and identified if it was above a threshold level of 20 virions/mL,

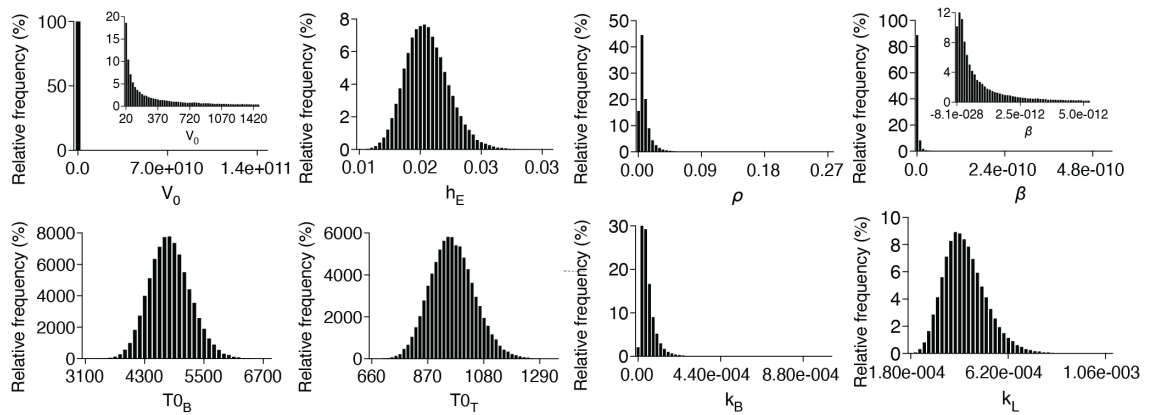


**Figure 3: Representative log-normal distributions of simulation parameters used in Monte Carlo method, given  $N = 100,000$ .**

matching the limit of detection of popular diagnostics [69]. Then, we recorded the occurrence of infection as a binary metric. This simulates an individual getting tested for HIV 18 days after exposure, which is the median p24 HIV test window period of fourth generation laboratory tests recommended by UK and US guidelines [70]. The data obtained was divided into 10 batches of 10,000 simulations each to enable statistical comparisons. The POI in each batch was calculated by dividing the number of positive infections by the size of the batch population. Due to the large number of simulations required, we took advantage of MATLAB's parallel computing capabilities and ran our simulations in nodes of Duke University's computing cluster.

## 2.2.9 Solving the Equations Numerically

All equations were solved numerically using the built-in equation solver for stiff ordinary differential equations `ode15s` in MATLAB. The equations were discretized in space to 1000 elements and converted into difference equations using the central difference method. This allowed us to solve the equations in time as if they were ordinary differential equations.

### 2.2.10 Exploring Effects of TFV Administration and User Adherence on Infection

To study the effects of user adherence, we ran our model using Monte Carlo simulations for 4 conditions: 1. no drug added, 2. drug added concurrently with exposure, 3. drug administered prior to exposure, and 4. drug administered after exposure. This approach allows us to study how protection via TFV varies depending on the timing of administration. This is important because on development, TFV gel was intended as an on-demand product. However, user application varies greatly, and it is important to know if product performance is robust to this variability.

The case where no drug is added is straightforward. However, for the cases where drug is added, we diluted the concentrations to reflect the volume ratios of gel, semen and vaginal fluid. For example, if drug is administered  $\alpha$  hours prior to exposure, the drug concentrations for the drug and virus follow the initial conditions:

$$C_{TFV,L}(x, 0) = C_0$$

$$C_{V,L}(x, 0) = 0$$

At  $t = \alpha$ , however, the concentrations in the lumen become:

$$C_{TFV,L}(x, \alpha) = C_{TFV,L}(x, \alpha - dt) \frac{V_g}{V_f + V_s + V_g}$$

$$C_{V,L}(x, \alpha) = V_0 \frac{V_s}{V_f + V_s + V_g}$$

By contrast, if drug is added  $\gamma$  hours post exposure, the initial conditions are:

$$C_{TFV,L}(x, 0) = 0$$

$$C_{V,L}(x, 0) = V_0$$

At  $t = \gamma$ , the concentrations in the lumen become:

$$C_{TFV,L}(x, \gamma) = C_0 \frac{V_g}{V_f + V_s + V_g}$$

$$C_{V,L}(x, \gamma) = C_{V,L}(x, \gamma - dt) \frac{V_s}{V_f + V_s + V_g}$$

Finally, in the case that drug is added approximately simultaneous to HIV exposure, the initial condition is simply:

$$C_{TFV,L}(x, 0) = C_0 \frac{V_g}{V_f + V_s + V_g}$$

$$C_{V,L}(x, 0) = V_0 \frac{V_s}{V_f + V_s + V_g}$$

We tested these conditions when drug was applied 4 and 2 hours before sexual HIV exposure, and 2 and 4 hours after sexual HIV exposure.

### **2.2.11 Analyzing The Susceptibility To Infection At Different Stages In The Menstrual Cycle**

To study the influence of the menstrual cycle, we focused on adjusting parameters, namely  $h_E$  and  $T_{0,S}$ , to fit the follicular phase, the luteal phase and midcycle. The average thickness of the epithelium was changed to  $150\mu\text{m}$  to simulate the follicular phase, and  $100\mu\text{m}$  to represent the late luteal phase, following experimental measurements by others [49]. Similarly, the cell density of target T cells in the vaginal stroma during the luteal phase was doubled to  $2000\text{cells/mL}$ , while in the follicular phase and at midcycle this density was kept constant at  $1 \times 10^3$  cells/mL. This follows observations that there was an increased CD4+ T cell density in the vaginal tract during the luteal phase, particularly during days 18-24 [48]. We ran our model for these three stages in the menstrual cycle and compared the ultimate POI in the absence and presence of drug, in this case applied concurrently to infection.

## ***2.3 Results and Discussion***

### **2.3.1 Viral Load and Cell Densities Throughout Infection Process**

The dynamics of sexual HIV transmission in the tissue of the female reproductive tract and in the blood is nuanced, but the outcome can generally be grouped into three buckets: no infection, infection that begins in the stroma and propagates out to the rest of the vaginal environment and to the blood, and infection that initiates in the blood stream, and later propagates into the vaginal environment. The details of this infection are highly sensitive to the complex parameter space. Figure 4 shows representative examples fitting these three buckets. We observe that when infection occurs, the viral load in tissue grows exponentially, beginning at the top of the stroma and progressing to the remaining tissue, including the epithelium, and even up to the lumen, indicating transport of virions to vaginal fluid as well. When infection does not occur, the viral load only marginally increases at the top of the stroma and then gets cleared away (Figure 4A,B). These findings match experimental observations of shallow penetration of HIV into vaginal tissue [55]. Cell populations in tissue and blood remain unchanged (Figure 4C,D).

The cell densities in tissue and blood match predictions from prior models of viral dynamics. Importantly, however, the fluctuations in these populations follow the circumstances of infection. If infection occurs first in the vaginal submucosa, we observe that the viral load in tissue begins to flare up first (Figure 4F). This causes a drop in the target cell population in the stroma (Figure 4G). Once the infection propagates into the blood (Figure 4F), the viral load in this compartment begins to rise and the population of target cells follows suit, lagging by up to several days (Figure 4H). In contrast, if infection occurs first in the blood, we see the situation reverse, with the viral load shooting up in

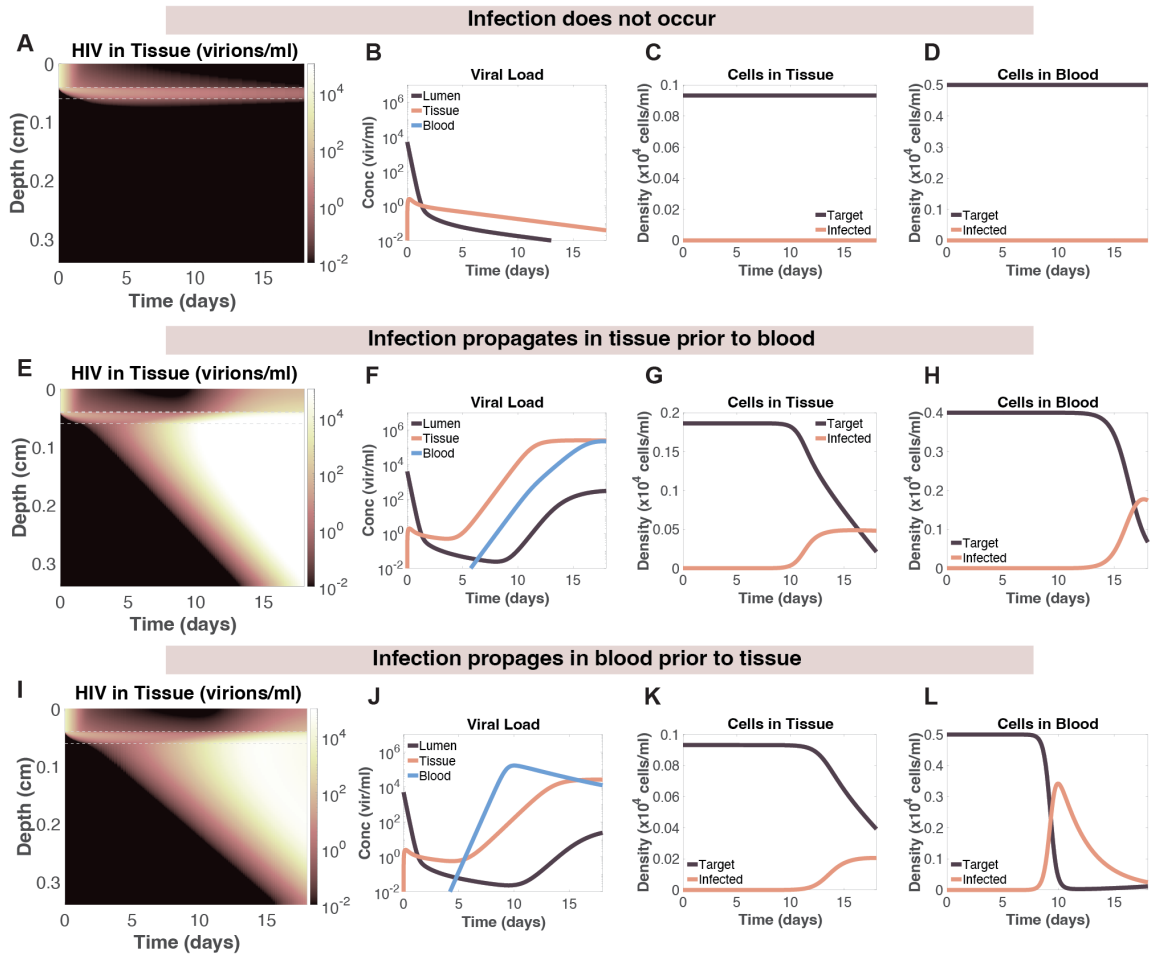


**Figure 4: Representative viral loads and cell densities for 3 cases:**

**No infection (A-D), positive infection propagating first in the vaginal stroma (E-H), and infection propagating in the blood before progressing to vaginal tissue (I-L). A,E,I: Heatmap of viral number density over time in the vaginal tract, including the lumen, epithelium and stroma. The dashed grey lines delineate the epithelium, with the lumen above the top line and the stroma below the bottom line. As time progresses, the viral density either exhibits exponential and propagates the infection or diminishes and subsides. A exhibits a situation where no infection occurs. E and I are examples of infection propagates. B,F,J: Average viral load in the lumen, tissue (including the epithelium and stroma) and in the blood compartment. B shows an example where no infection occurs, in F and J infection does occur. C,G,K: Average number densities of target and infected cells in the tissue. When infection propagates, the density of target cells drops rapidly, and the density of infected cells rises. When no infection occurs, the cell densities remain unchanged. D, H and L: Average number densities of target and infected cells in the blood. Infection causes the density of target cells to increase substantially. The density of infected cells also increases substantially at the onset of infection, but eventually starts to decrease due to the reduced number of healthy cells available for infection.**

the blood first, leading to rapid changes in blood target and infected cell densities, while

the viral load and cell density in the tissue lag behind. The implication of infection occurring first in the blood is important. This situation occurs often given that the density of infectible target cells is significantly higher in the blood than it is in the stroma. Further, if the rate of viral transfer from the stroma to the blood is high, this also increases the likelihood of infection originating in the blood. This critically limits the efficacy of topically applied microbicides. These products can effectively protect immune cells in the vaginal environment, where they are locally delivered. However, for TFV, drug molecules do not permeate into the blood at sufficiently high concentrations to provide protection in the bloodstream. If virions permeate into the bloodstream at sufficiently high concentrations, infection is likely to occur irrespective of the intravaginal administration of the TFV gel.

### **2.3.2 Effect of Drug Administration on the POI**

TFV distributions in vaginal tissue, when the drug is delivered via a topically applied gel, follows classic PK curves, as we have observed in our prior models [28]. Heatmaps of the distribution of TFV show that the drug can permeate into the stroma within the span of a few hours (Figure 5A, 5D), and then slowly gets either removed from the stroma or phosphorylated into TFV-DP. When in this form, the drug can remain in tissue for significantly longer (Figure 5B, 5E). Here, we use the drug's dose response curve (Figure 5F) to map the concentration of TFV-DP in tissue to  $q$ , a parameter that represents the drug efficacy, bound between 0 and 1. The heatmap of  $q$  shows high protection in the epithelium, and elevated protection in the order of several days in the stroma (Figure 5C). However, deeper into tissue, the lower the level of protection provided by TFV-DP and the faster it diminishes over time. TFV can leave the tissue and enter the bloodstream. However, given the small volumetric average of cells in the blood, conversion to TFV-DP is inefficient, and not enough to achieve any significant

level of protection (Figure 5E). As elaborated in the previous section, this means that if HIV enters the bloodstream, there is no level of protection provided by the intravaginally delivered anti-HIV drug TFV.

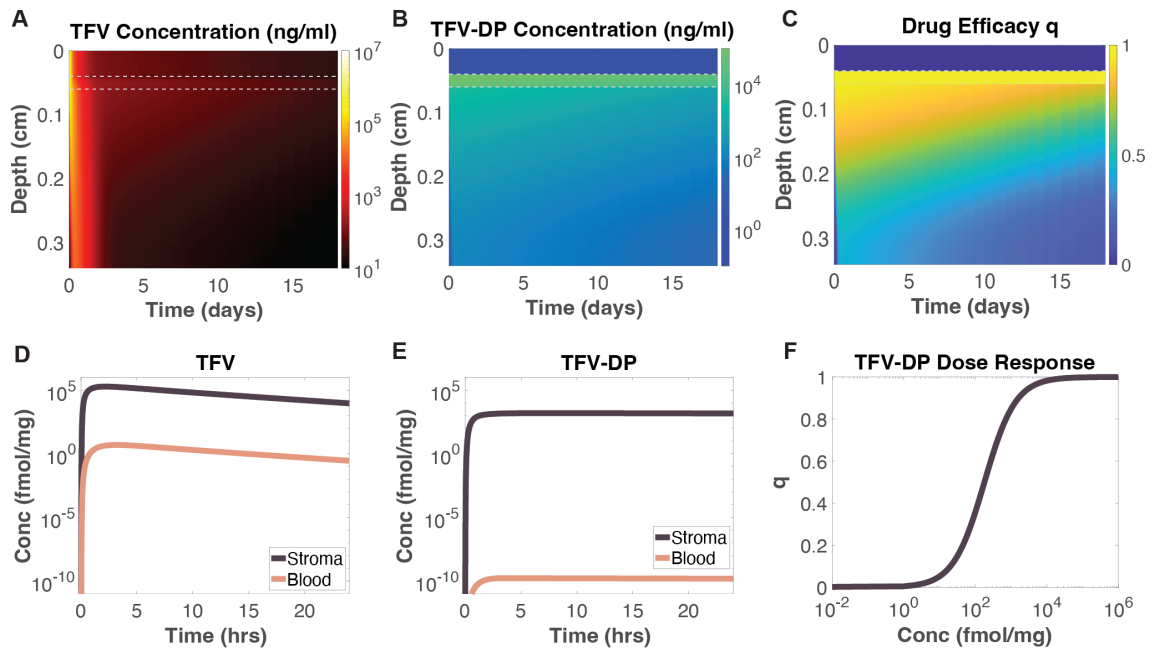


**Figure 5: Distribution of drug molecules and efficacy throughout the domain.**

**A:** Concentration of TFV in the vaginal tract across time. The dashed lines delineate the epithelium, with the lumen above the top line and the stroma below the bottom line. The color of the heatmap corresponds to TFV concentration and is in log scale. **B:** Concentration of TFV-DP in the vaginal tract across time, including the lumen, the epithelium (delineated by the dashed lines) and the stroma below. The color of the heatmap corresponds to the concentration of TFV-DP and is in log scale. **C:** Drug efficacy,  $q$ , in the vaginal tract across time, calculated by mapping the spatiotemporal concentration of TFV-DP to its dose response curve. **D:** Volume-averaged TFV concentration in the stroma and in the blood. The concentration in the blood is significantly lower than that in the tissue. **E:** Volume-averaged TFV-DP concentration in the stroma and blood. In the blood, the concentration of TFV-DP is negligible. **F:** Dose-response curve of TFV-DP calculated via equation 8. Drug efficacy  $q$  is obtained by mapping the concentration of TFV-DP in the tissue or in the blood into this function.

The predicted POI for a situation in which no drug was applied was estimated at 0.23%. This is a slight overestimation relative to the average reported values for receptive vaginal sex, at 0.08% [71]. One possible reason for this is the choice of

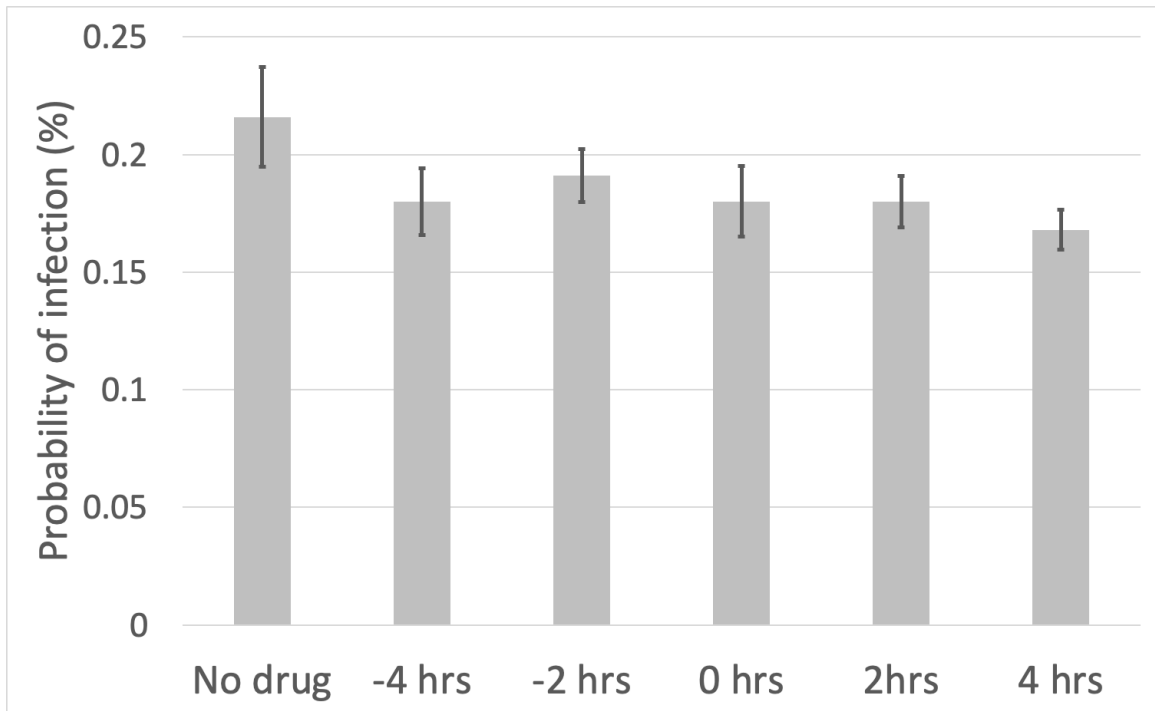


**Figure 6: Probability of Infection (POI) relative to different drug administration conditions at midcycle.**

**Labels in the x-axis corresponds to timing of drug application relative to HIV exposure. Error bars show the standard error. A 1-way ANOVA was performed to test differences associated with the condition of drug administration. No statistically significant differences were found, although in general the trend shows that the presence of TFV, irrespective of the timing of administration, reduced the POI by an average of 16.8%.**

parameters, specifically the infectivity of virions  $\beta$ , the production rate of new virions from infected cells  $\rho$  and the and the rate of cell-to-cell infection  $\omega$ . These values have been estimated in the literature by fitting viral dynamics models to a biased population of women that were HIV+. However, in our case, we are attempting to achieve a generalized POI with a balanced, unbiased population, of which we expect the majority to not be infected by HIV. For this purpose, we reduced our estimates of both  $\beta$  and  $\omega$ , but the chosen values may have still been an overestimation. Reducing both parameters further would result in lower values of the POI that may better fit data in the literature.

In our analysis of user adherence and TFV gel administration, we found that on average, the POI was reduced by 16.8% when the TFV gel was administered (Figure 6), irrespective of the timing of drug administration. This reduction matches ranges measured in clinical studies [6]. However, no statistical significance was found when comparing the POI for cases of no drug application and drug administration at varying timepoints relative to HIV exposure. This may indicate a limited reduction in the POI by a TFV gel due to only reducing free virus-to-cell infection but not influencing cell-to-cell infection, which is the dominant means by which infection propagates [72-74].

#### **2.3.4 Susceptibility to Infection During the Luteal Phase and Follicular Phases of the Menstrual Cycle**

Throughout the menstrual cycle, variations in steroid hormone levels result in physiological changes in the female reproductive tract, including the vagina. We addressed the consequences of these in our model. We distinguished the follicular cycle phase (post menses, where estrogen rises) vs. the luteal phase (post ovulation, where progesterone levels rise). In the vagina, the hormone changes induce variations in the thickness of the epithelium and the number and phenotype of CD4+ immune cells in vaginal tissue [48-50]. In our model, this would correspond to changes in  $h_E$  and  $T_{0,S}$ , the initial cell density of infectible target cells in the stroma. Studies also suggest that the stage of the menstrual cycle changes the volume and viscosity of mucus that leaks from the cervical os into the vaginal lumen, thereby influencing drug and viral transport [75, 76]. Since HIV is significantly larger than TFV molecules, more viscous mucus would slow down viral transport more than it would drug molecules. In our model, this would be reflected by a reduction in the diffusion coefficients  $D_{V,L}$  and  $D_{TFV,L}$ . Further, changes in the rate of vaginal fluid production may lead to faster loss of virions and drug molecules

in the lumen,  $k_{TFV,D}$  and  $k_{D,V}$ . For our analysis, we adjusted  $h_E$  and  $T_{0,S}$ , assuming a thicker epithelium and a higher number density of target cells in the stroma during the

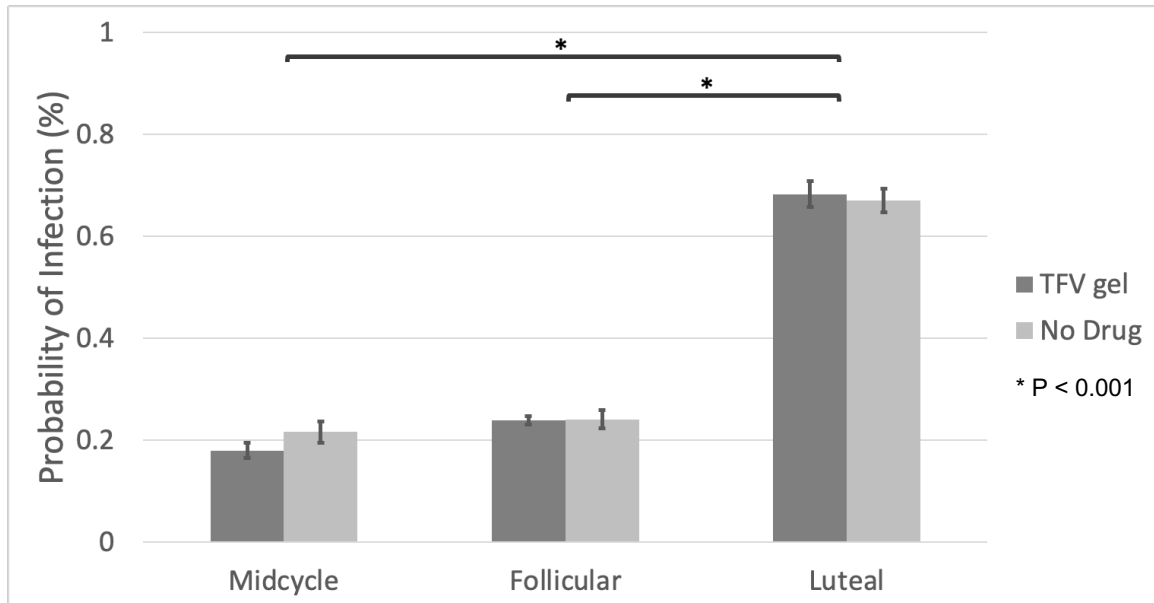


**Figure 7: Probability of Infection (POI) during the follicular phase, luteal phase and at midcycle in the presence and absence of drug administration, for the case where drug is applied simultaneous to HIV exposure.**

The error bars show standard errors. We ran a 2-way ANOVA to analyze the effects of menstrual cycle phase and drug presence on the POI and followed up with Tukey’s HSD for multiple comparisons.

follicular phase relative to the luteal phase, following prior studies [48-50]. However, it is difficult to quantitatively correlate the changes in vaginal mucus composition with the diffusion coefficients and loss terms in the lumen. Therefore, in our analysis we kept these parameters constant for simplicity.

The results of our ANOVA for the conditions in Figure 7 suggest that the POI did not vary significantly between no drug and administered TFV gel cases, for the case of gel administration followed immediately by semen deposition. This is an example of

application of the model but does not reflect all conditions of human use (Figure 6). However, there were statistically significant differences amongst the different menstrual cycle phases. More specifically, the probability of HIV infection during the luteal phase was 70.8% higher than at midcycle, and 64.5% higher than at the follicular phase (Figure 7). In our simulation, the luteal phase was assumed to have on average half the thickness of the epithelium compared to midcycle, and a CD4+ T cell density that was twice the cell density at midcycle. In contrast, the follicular phase had the same target cell density in the stroma as midcycle, but also had a 33% thinner epithelium. Although the POI differences between the follicular and midcycle phases were not statistically significant, there was a higher POI during the former as compared to the latter. During our tests, we found that the estimations of the POI weren't that sensitive to the epithelial thickness due to the lack of a loss term in this layer, meaning that virus and drug molecules would eventually make it through irrespective of thickness. However, the results shown here emphasize the deep dependence of the POI on the density of infectible immune cells in the tissue. Indeed, several studies have reported an increase in susceptibility to HIV infection during inflammatory periods in the vaginal environment, which occur periodically during the menstrual cycle. However, the correlation with the exact phase of the menstrual cycle is mixed, with some studies shown an increase in frequency of infection events during the follicular phase [49, 77, 78], and others indicating higher susceptibility during the luteal phase, particularly in the late luteal phase [48, 79]. To make our analysis more conclusive, a more detailed exploration of parameter space should be performed, playing close attention to phenomena that we are currently assuming negligible, including hormonal effects on vaginal mucus, which may also play a significant role in the incidence of infection.

### 2.3.6 Limitations of the Study

The model built here is an effective tool to study the heterogeneous, spatiotemporal dynamics of HIV infection in the vagina following sexual exposure to HIV. However, the model does slightly overestimate the POI in the absence of drug. One possible reason is the choice of the parameter means used in the Monte Carlo simulations. These parameters, estimated from data in the literature, are biased towards populations where infection did occur, and are not balanced to a generalized population of at-risk women. A more nuanced sensitivity analysis would allow us to fit these parameters such that the predicted POI better matches expected results. Despite the discrepancies on the absolute value of this computation, predictions of relative differences of the POI and its dependence on drug administration conditions to match results in the literature [6]. To build this model, we also assume that infection occurs instantaneously at the onset of HIV-cell interactions. However, studies suggest that there is a meaningful intracellular delay that defers infection and the production of new virions from infected cells [80]. Accounting for this mechanism may lower the POI as well, as it would lengthen the time for other processes, including cell death and drug protection, to occur before new virions are produced by infected cells.

One key assumption made in our model is 1-dimensional diffusion within the vaginal environment. This assumption is valid given that the rate of transport downwards into the tissue is significantly faster than longitudinally along the length or width of the lumen and submucosa. However, in the lumen, there usually is slow convective transport towards the introitus as vaginal fluid is produced and moves down the vaginal canal [30, 81]. If vaginal fluid is being produced at sufficiently high rates, for example during certain periods in the menstrual cycle, this transport may become significant and

cause heterogeneity in transport along the length of the tract as well. In our exploration of the susceptibility to infection in the follicular vs. luteal phase of the menstrual cycle, including the details of this phenomenon, in addition to changes in parameters resulting from varying mucosal viscosities and compositions, would improve the accuracy of our predictions.

Finally, in our analysis we include only the vaginal environment and the bloodstream, which are fundamental to analyzing the risk of sexual HIV transmission in women. However, sexual HIV infection also occurs readily in cervical tissues [82], and propagates readily in lymph nodes, which have a high density of infectible immune cells [83, 84]. Including these compartments would exponentially increase the complexity of the model and the number of parameters, but it would also enable a more complete analysis of the dynamics of infection under the influence of microbicide administration.

## ***2.4 Conclusion***

We have built a mathematical framework that couples together viral transport, drug transport and viral dynamics to estimate the POI as a key PD metric over which we can computationally test and compare different anti-HIV microbicide products. The model allows us to make powerful mechanistic observations on the dynamics of infection and uncovers significant insights such as the possibility of infection occurring in the bloodstream before it does in the vaginal submucosa. Using this model, we tested a topically applied TFV gel and found, over a range of timing of gel application, that it reduces the POI by 16.8% on average. This is consistent with the results of the CAPRISA clinical study [46]. The timing of drug administration relative to HIV exposure may affect the POI, depending upon the cycle phase. Our analysis indicated that the POI

was highest in the luteal phase and lowest at midcycle. Although we chose TFV as an initial proof-of-concept test due to the abundance of data available, our mathematical formulation can be applied to any topically applied microbicide molecule, if there is an understanding of its transport properties, its mechanism of action, and its dose-response. Our model also enabled a mechanistic interpretation on the impact of the menstrual cycle on susceptibility of infection. The cell density of immune cells in the stroma, which could increase with inflammation, had a significant impact on the POI. Ultimately, the model presented here could provide value to inform the mechanics of the infection process and the design of novel topically applied anti-HIV microbicide products.

## **3. Modeling Phase-Transitioning Therapeutic Injections into Superficial Solid Tumors**

### ***3.1 Background and Context***

In low- and middle- income countries (LMICs), limited access to surgery and other cost-prohibitive cancer therapies like chemotherapy and radiation make it increasingly difficult to get appropriate treatment. This issue is exacerbated by the lack of access to proper diagnostics, resulting in cancers being diagnosed at later, more advanced stages, when there is greater urgency [85]. There is a need for low-cost cancer diagnostics and treatment options. To address this issue, our collaborators proposed tumor ablation via intratumoral injections of ethanol-ethyl cellulose as a viable and promising inexpensive treatment strategy, exhibiting efficacy in hamster cheek-pouch tumor models [10] and breast tumor rat models [11]. It is currently being investigated for cervical, liver, and breast tumors [12, 13, 15].

In these injections, ethanol is the necrotic agent and ethyl cellulose behaves as a sustained-release agent that phase-separates to form a slow-release depot that minimizes leakage to non-target tissues. Ethyl cellulose is an ethanol-soluble, water-insoluble polymer that phase separates from a liquid phase to a dense, gel-like solid when in contact with water [10]. Ethanol causes necrosis via dehydration of the cellular cytoplasm and protein denaturation [86].

To optimize the efficacy of these injections in the various tissues in which the method is being tested, it is necessary optimize salient injection parameters in a tissue-specific manner. This requires having a mechanistic understanding of the various solid mechanics and transport phenomena occurring throughout the injection process. Experimental studies of ethanol-ethyl cellulose injections using IVIS, CT imaging,

fluorescence microscopy, Raman spectroscopy and histological staining [12-15] have teased out some of these relationships, but they provide only discrete snapshots of processes governed by continuously varying parameters. As such, they are limited in their abilities to explore the complex parameter space underlying these injections. Our goal in the work here was to develop a tool that would enable such parameter exploration. To this end, we developed a deterministic, mechanistic mathematical model that facilitates parameter analysis, and that provides a way of testing injection parameters on tissues with different properties. The following sections present and discuss this model, what its computations can predict, its strengths, and its limitations. We kept the model simplified and generalized to keep it applicable to injections of ranges of tumor- ablative or necrotic agents, and of co-injected phase-separating agents. However, in section 3.4.1 we discuss strategies to apply it to ethyl-cellulose injections in specific tissue types, including cervical, liver and breast cancer tissues.

### ***3.2 Introduction***

Localized intratumoral injections of necrotic agents, immunotherapeutics, and chemotherapeutics, have been studied extensively for treatment of superficial tumors and lesions [87-90]. This strategy is motivated by the potential for non-invasive therapies with increased efficacy, due to targeted, contained delivery of the active pharmaceutical ingredient (APIs) within the tissues of interest, as well as reduced systemic side effects. However, the efficacy of this approach is hindered by a lack of control over the transport of the API throughout tissue, which often leads to unintended outflow from the tumor into healthy tissue, and lower concentrations of the necrotic agent inside the tumor [91]. Inefficient containment of the API within target tissue may result from three main causes:

1. unintended rapid convective-diffusive transport of the API through the poroelastic tissue during and after the injection ends; 2. unintended leakage of the injectate through natural conduits with low resistance to flow, for example through blood vessels and lymphatics; and 3. unintended leakage through fractures in tissue which are created during needle insertion and/or throughout the injection when the local hydrostatic pressure exceeds a critical pressure of the tissue. To overcome these issues, a common strategy is to co-deliver the API with an agent which slows down transport, such as a fluid that solidifies within the target environment, to help contain the API and occlude conduits for leakage. These release agents may include hydrogels that undergo gelation within the target tissue due to pH or temperature responsiveness, or water-insoluble materials that phase-separate within the aqueous tumor environment [92]. For example, injections of ethanol-ethyl cellulose mixtures have shown promise for potential inexpensive tumor-ablation therapies, due to improved local retention of ethanol, the ablative API, within the margins of the tumor [10]. However, the dynamics of gelation or phase separation of the injectate within the aqueous tumor environment, and their impact on injectate distribution and retention, are poorly understood at present.

During an intratumoral injection, the increased hydrostatic injection pressure causes a poro-viscoelastic deformation in tissue, resulting in an injectate-filled cavity at the needle tip. This cavity grows as more fluid is injected, with a portion of the injectate fluid permeating into the porous tissue. If the pressure at the boundary of this cavity exceeds the critical pressure of the tissue, the tumor may fracture and cause leakage. Similarly, leakage may occur in regions of the tissue that were damaged during needle insertion, such as those abutting the walls the needle. All these phenomena occur simultaneously, resulting in a complex overall process influenced by injection

parameters such as flow rate, injected volume and needle insertion depth, tissue-specific parameters including porosity, elasticity and intrinsic permeability, and physicochemical properties of the API and its delivery vehicle, including molecular size, hydrophobicity and viscosity, throughout and after the course of the injection. A cartoon depicting the injection process is shown in Figure 8.

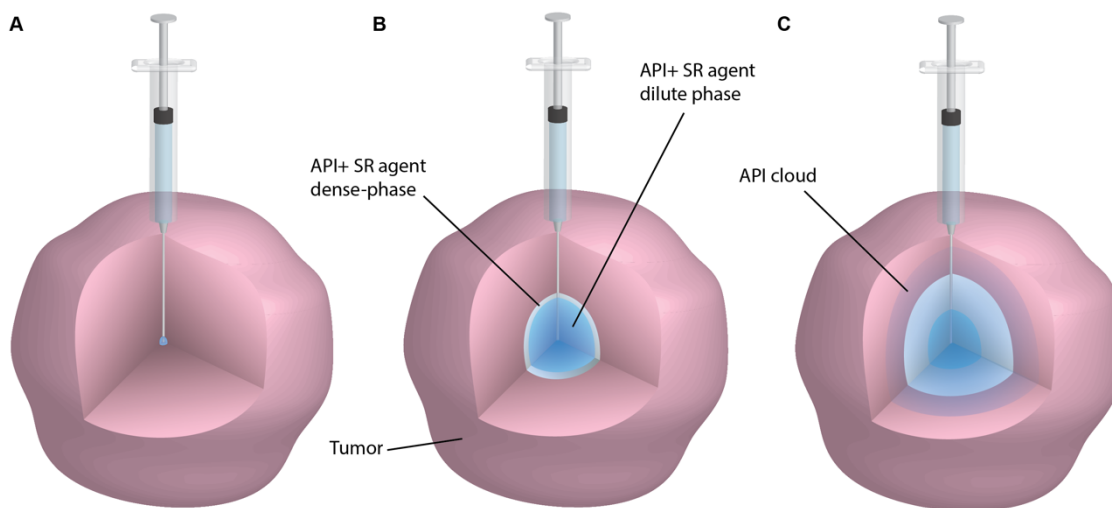


**Figure 8 Representative cartoon of injection process.**

**A – At  $t = 0$ , initially cavity has a radius equal to the needle’s inner radius. B – Some time  $dt$  afterwards, the radius has grown due to the injection pressure. The sustained release (SR) agent begins to phase-separate, forming a shell at the boundary of the cavity. The inside of the cavity is still full of the API and the dilute phase of the SR agent. C – Due to convection and diffusion, the API is released from the cavity through the dense phase of the SR agent. The transport rate of the API is influenced by the presence of the SR dense phase.**

Deterministic mathematical models of these injections can inform and facilitate exploration of their complex parameter space and provide a means to help predict and optimize the injection procedure. Prior models of intratumoral injections have focused on two simultaneous processes: the poroviscoelastic deformation of tissue driven by the injection pressure, and the convective-diffusive mass transport of the API into tissue from the injectate-filled cavity, which grows around the needle tip [18, 93]. Importantly,

these mathematical formulations have assumed the tissue to be linearly elastic. This is an appropriate approximation for small poroelastic tissue deformations in many tissues [18]. Prior studies have also often assumed that the critical pressure of tissue is not exceeded, such that fracture and leakage do not occur. This helps simplify the problem, which becomes a one-dimensional spherically symmetric biphasic model [18], where the radius of the cavity depends on the viscosity of the injectate, tissue poroelasticity and permeability, and on injection parameters such as flow rate and volume injected. These models provide a valuable means to explore drug pharmacokinetics (PK) under a range of conditions. However, as the development of anti-tumor injections moves to adding sustained release agents to increase local API retention (such as ethyl cellulose), the complexity of the system is magnified, and more comprehensive injection models become necessary. To our knowledge, there is currently no mathematical framework for intratumoral injection that accounts for spatially and temporally dependent gelation or phase separation of a sustained release agent in the injection formulation.

Cahn Hilliard theory describes the process of phase separation of a multi-component mixture, usually a binary mixture, from a single thermodynamic phase to two or more individual phases, driven by a chemical potential [94-96]. Here, we use this theory to model the presence of a dilute liquid phase and a dense solid phase within the injection cloud, where the dilute phase is a mixture of the injected drug solution and the liquid sustained release agent, and the solid phase consists of the gelled or phase-separated sustained release agent. The Cahn Hilliard model outputs a phase-field 'order' parameter, which represents the phase constitution with spatiotemporal detail. In our model, this parameter ranges from -1 to 1, where the former describes the purely liquid phase, and 1 represents the dense phase of the sustained release agent. This

information feeds into the mass transport theory via a phase-dependent diffusion coefficient which we assume decreases linearly with the order parameter. This assumption is valid if we postulate that the effective local viscosity within the injection cloud increases linearly with the order parameter, and that the diffusion coefficient follows Stokes-Einstein theory and decreases linearly with that viscosity.

By integrating poroelastic tissue deformation, convective-diffusive transport of the API, and the phase separation of the sustained release agent in spatiotemporal detail, we create a general framework that enables first-pass exploration and optimization of injection procedures for local drug injection in tissue including a gelling or phase-separating sustained release agent.

## **3.2 Methods**

### **3.2.1 Problem Definition**

In this problem, we assume that a needle with inner radius  $r_0$  has been inserted into an isotropic poroelastic tumor to form a spherical cavity with an initial radius equal to the inner radius of the needle. Tumor tissue is modeled as a biphasic system consisting of fluid within solid poroelastic matrix, which we also assume to be spherical. We also assume that the tumor tissue is surrounded by a layer of healthy tissue. The symmetry in the geometry allows us to model this problem in 1D spherical coordinates.

The injection progresses in two phases: the fluid injection phase, and the relaxation phase. During the fluid injection phase, a prescribed volume  $V$  of a mixture including the API and the gelling agent in its liquid phase is injected through the needle at a fixed flow rate  $Q$ . We assume that the tissue is semi-permeable to the API, but the gelling agent precipitates instantaneously at the tissue interface (i.e., in negligible time

relative to the time scale of the injection) and does not permeate into the porous tissue matrix. Due to the pressure field, the solid tissue matrix deforms as a function of  $Q$ , the hydraulic conductivity  $K$  and the elastic properties of the tissue, which we characterize via the Lamé parameters  $\mu$  and  $\lambda$ . This deformation is characterized by the dilatation of the solid  $e$  and a solid displacement field  $u$ . The API's transport throughout the domain, including the cavity, tumor, and surrounding healthy tissue, occurs via convection and diffusion. The convection component is governed by the fluid velocity field  $v_f$ , which depends on the rate of solid displacement. Diffusion on the other hand, occurs at a fixed rate through tumor and healthy tissue, but varies as a function of the phase composition of the precipitating agent inside the cavity. The API diffuses more slowly in precipitated dense-phase material vs. in dilute, liquid phase material, and we assume this relationship to be linear. Once the full volume of the mixture has been injected, at  $t > V/Q$ , the injection phase ends, and we progress to the relaxation phase. At this stage, we assume that pressure and fluid velocity drop to 0 in negligible time relative to the time scale of the injection. We also assume that the radius of the cavity stays fixed, as it is kept open by the dense phase of the sustained release gelling agent. Phase separation of this agent and API diffusion also continue during this phase.

Ultimately, three fundamental physical mechanisms progress during both the injection and relaxation phases: soft tissue deformation; gelling agent phase separation; and mass transport of the API through the domain. These processes are coupled: the cavity that grows because of tissue deformation behaves as a moving boundary that affects the precipitation process as well as API mass transport, and the fluid velocity that depends on tissue deformation directly affects the convective transport of the API. Here

we present a framework that couples these three physical mechanisms into a system of partial and ordinary differential equations that are solved numerically.

### 3.2.2 Biphase Poroelastic Tissue Deformation

The continuum mechanics of tissue deformation follow the mathematical framework originally developed by Mow et al., and further explored by Netti et al. [16-18]. Briefly, we assume tissue to be homogenous biphasic system with a solid and a fluid phase, and thus set up the governing mass and momentum balance equations for the fluid and solid phases as a function of  $\Phi$ , the volumetric fraction of the fluid phase (equations 30-32). Governing equations are listed below:

Mass Balance:

$$\nabla \cdot \left( \Phi v_f + (1 - \Phi) \frac{\partial u}{\partial t} \right) = 0 \quad (30)$$

Momentum Balance:

$$\nabla \cdot \sigma^f + \nabla \cdot \sigma^s = 0 \quad (31)$$

$$\Phi \left[ v_f - \frac{\partial u}{\partial t} \right] = -K \nabla p \quad (32)$$

Importantly, in this calculation we assume infinitesimal strain theory to be valid such that tissue behaves as a linearly elastic material for infinitesimally small strains. This allows us to set a constant hydraulic conductivity. Although allowing hydraulic conductivity to be a function of the deformation would be more accurate, for the purpose

of this analysis, where the magnitude of the solid displacement field is small relative to the dimension of the tumor tissue, this assumption is an appropriate starting point.

The Cauchy stress tensors for the fluid and solid phases of tissue are given by finite deformation biphasic theory. The fluid phase stress tensor consists of a hydrostatic term (equation 33), while the solid phase also incorporates an elastic term described by the Lamé parameters  $\mu$  and  $\lambda$ , the deformation tensor  $\epsilon$ , and the solid dilatation  $e$  (equation 34).  $e$  is the trace of  $\epsilon$  (equation 35), where the deformation tensor  $\epsilon$  is given by equation 36. Constitutive equations are listed below:

$$\sigma^f = -\Phi p I \quad (33)$$

$$\sigma^s = -(1 - \Phi)p I + 2\mu\epsilon + \lambda e I \quad (34)$$

$$e = \text{tr}(\epsilon) = \nabla \cdot u = \frac{\partial u_r}{\partial r} + \frac{2u_r}{r} \quad (35)$$

$$\epsilon = \frac{1}{2} [\nabla u + (\nabla u)^T] \quad (36)$$

As boundary conditions, we impose negligible dilatation at the end of the domain  $r = R$  (equation 8), and a constant velocity at  $r = r_0$  that is simply the constant injection flow rate  $Q$  divided by the spherical cross-sectional area (equations 37,38). Finally, we also assume that the partial solid stresses on the surface of the cavity, at  $r = r_0$  are 0 (equation 39). Initially, the dilatation,  $e$ , is zero everywhere (equation 40). Boundary conditions and initial condition equations are listed below:

$$e(r = R, t) = 0 \quad (37)$$

$$v(r = r_0, t) = \frac{Q}{4\pi r_0^2} \quad (38)$$

$$\tau_{rr}(r = r_0, t) = 2\mu \frac{\partial u_r(r = r_0, t)}{\partial r} + \lambda e(r = r_0, t) = 0 \quad (39)$$

$$e(r, t = 0) = 0 \quad (40)$$

When combining the governing equations with the constitutive equations, we obtain a system of equations (equations 41-43) that can be solved to obtain the solid displacement field  $u$ , the dilatation  $e$ , and the pressure field  $P$ . The fluid velocity  $v_f$  can then be computed from equation 32. Simplified equations are listed below:

$$(\lambda + 2\mu)\nabla e(r, t) = \nabla p(r, t) \quad (41)$$

$$\frac{\partial e(r, t)}{\partial t} = K(\lambda + 2\mu)\nabla^2 e(r, t) \quad (42)$$

$$e(r, t) = \nabla \cdot u(r, t) = \frac{1}{r^2} \frac{\partial}{\partial r} (r^2 u_r) \quad (43)$$

### 3.2.3. Phase Separation of the Gelling Agent

The phase separation of the gelling agent is modeled using Cahn Hilliard theory, which provides a continuum, phase-field approach to characterizing and computing the

phase separation of the gelling agent [94]. A key advantage of applying this theory is that it captures diffuse interfaces between components in a mixture, which enables computation of smooth variations in key phase-dependent properties through space and time. In our problem, an example of such a property is the diffusion coefficient of the API in the cavity, which is dependent on the phase of the gelling agent and directly influences API mass transport dynamics. The phase of the phase separating agent is given by the order parameter  $\varphi(r, t)$ , where  $\varphi \in [-1, 1]$ . When  $\varphi(r, t) = -1$ , the gelling agent is in its pure dilute, liquid phase, whereas when  $\varphi(r, t) = 1$ , its in its pure gelled state. Equation 44 shows the governing equation that is solved to compute  $\varphi$ , where  $M$ , the mobility coefficient, controls the speed of the phase separation reaction, and  $\mu_\varphi$  is the chemical potential driving the precipitation process. Although  $M$  can be a function of  $\varphi$ , in our analysis we assume it to be constant for simplicity.

$$\frac{\partial \varphi}{\partial t}(r, t) = \nabla \cdot [M(\varphi(r, t)) \nabla \mu_\varphi(r, t)] \quad (44)$$

The chemical potential is given by equation 45 and is derived by calculating the derivative of the total free energy functional with respect to  $\varphi$ .

$$\mu_\varphi(r, t) = F'(\varphi(r, t)) - \varepsilon^2 \Delta \varphi(r, t) \quad (45)$$

$F(\varphi)$  is a double well potential for a homogenous binary mixture with composition  $\varphi$ , and is given by constitutive equation 46.

$$F(\varphi(r, t)) = 0.25(\varphi(r, t)^2 - 1)^2 \quad (46)$$

$\varepsilon$  is a positive constant that defines the contribution of interfacial energy to the total free energy of the system. The radius of the cavity behaves as a moving boundary that affects the dynamics of the phase separation process. At  $r = r_c$ , on the cavity surface, we assume that the gelling agent phase-separates instantaneously, so we apply a constant boundary condition of  $\varphi = 1$  at this interface across all values of time (equation 47).

$$\varphi(r = r_c, t) = 1 \quad (47)$$

Initially, the inside of the cavity excluding the interface is assumed to be full of the liquid phase of the gelling agent, so we set  $\varphi = -1$  as an initial condition within this domain (equation 48).

$$\varphi(r \neq r_c, t = 0) = -1 \quad (48)$$

### 3.2.4 API Mass Transport

Mass transport of the API is governed by the convection diffusion equation (equation 49).

$$\frac{\partial c}{\partial t}(r, t) = \nabla \cdot [D(\varphi(r, t))\nabla c(r, t)] - \nabla \cdot (v_f c) \quad (49)$$

The fluid velocity is obtained from equation 3, as it directly relates to tissue deformation. In the relaxation phase, this velocity is assumed to instantaneously drop to 0. Diffusion progresses during both the fluid injection and relaxation phases and is modulated by the diffusion coefficient. In the tissue, this parameter is constant, but in the cavity it depends on the order parameter  $\varphi$  that captures the phase of the gelling agent. Here, we assume that given constant diffusion coefficients for orders  $\varphi = 1$ , and  $\varphi = -1$ ,  $D_{c,dense}$  and  $D_{c,dilute}$  respectively, we can estimate the diffusion coefficient at any other intermediary value of  $\varphi$  via a linear relationship (equation 50). The diffusion coefficient in the tissue is constant (equation 51). The constitutive equations are listed below:

$$D(\varphi(r, t)) = \frac{1}{2}(D_{c,dense} - D_{c,dilute})(\varphi + 1) + D_{c,dilute}, \quad r \leq r_c \quad (50)$$

$$D(\varphi(r, t)) = D_t, \quad r > r_c \quad (51)$$

This relationship assumes that the viscosity of the gelling agent increases linearly with phase, and that we can apply the Stokes Einstein relationship such that the rate of diffusion decreases linearly with viscosity. At  $r = r_c$ , we prescribe a partition boundary condition to account for possible varying solubilities of the API in the cavity and in the tissue (equations 52-53).

$$c(r = r_c^-, t) = P \cdot c(r = r_c^+, t) \quad (52)$$

$$D_c(\varphi(r = r_c^-, t)) \frac{\partial c}{\partial r}(r = r_c^-, t) = D_T \frac{\partial c}{\partial r}(r = r_c^+, t) \quad (53)$$

As the initial condition, we assume a zero API concentration for  $r > r_0$  and a constant concentration  $c_0$  in the space occupied by the tip of the needle (equations 54-55).

$$c(r > r_0, t = 0) = 0 \quad (54)$$

$$c(r \leq r_0, t) = c_0, 0 \leq t \leq \frac{V}{Q} \quad (55)$$

### 3.2.5 Parameter Choice

In our analysis, we systematically analyzed ranges of the multiple parameters. Reference (or assumed) values used in our simulations are shown in Table 4. The rationale for these reference values is explained below.

The partition coefficient  $P$  was assumed to be 1 for simplicity. The total size of the simulation domain  $R$  was set to 2cm, a biologically realistic value that was large enough to avoid boundary effects from significantly affecting simulation results.

The diffusion coefficient of ethanol in water has been measured to be on the order of  $10^{-5}$  cm<sup>2</sup>/s [97]. This provided us with an upper bound for the diffusion coefficient of ethanol in solution with liquid EC,  $D_{C,dilute}$ , which here we assumed to be an order of magnitude lower, at  $10^{-6}$  cm<sup>2</sup>/s. We have previously estimated the diffusion coefficient of

ethanol in tissue  $D_T$ , on the order of  $10^{-6}$  cm<sup>2</sup>/s [15]. However, due to the biphasic nature of tissue and the reduced permeability of the solid phase, we postulated that the diffusion coefficient in tissue should be lower than  $D_{C,dilute}$ , and so we assumed  $D_T = \frac{1}{2} D_{C,dilute}$  as a reasonable value. Finally, we assumed that the diffusion coefficient of ethanol in the solid EC phase,  $D_{C,dense}$ , was significantly slower than its counterpart in the dilute phase and set a conservative value of  $1 \times 10^{-8}$  cm<sup>2</sup>/s for this parameter. The lack of experimental measurements made parameter choices for these diffusion coefficients difficult, so our approach was to approximate reasonable averages and then test ranges of values in our analysis.

Due to the lack of quantitative experimental data, the choice of the mobility coefficient  $M$  and the interfacial parameter  $\varepsilon$  was made heuristically. We chose values that led to realistic phase separation profiles in space and time, with a shell of dense EC forming in the cavity over the span of 15 minutes, following empirical observations of injections into tissue. We also tested values of  $M$  within a wide range to test the sensitivity of injection efficacy to this parameter. In applications of the model, the values of  $M$  and  $\varepsilon$  should be modified to fit the specific composition of the injection and the phase-separation dynamics of the precipitating or gelating co-injected material.

**Table 4.** Default parameters used in intratumoral injection model

Description	Symbol	Value	Source
Hydraulic conductivity	$K$	3.8e-10m <sup>2</sup> /kPa	[18]
Tissue porosity	$\Phi$	0.2	[18]
Lamé's first parameter	$\lambda$	13.16kPa	[18]
Lamé's second parameter	$\mu$	6.58kPa	[18]
Flow rate	$Q$	1mL/hr	[10, 14]
Injection volume	$V$	0.5mL	[12]
Needle internal radius	$r_0$	0.03cm	[18]
Mobility coefficient	$M$	3e-11cm <sup>2</sup> /s	Assumed
Interfacial parameter	$\varepsilon$	0.2	Assumed
Diffusion coefficient in tissue	$D_T$	5e-7cm <sup>2</sup> /s	[15]
Diffusion coefficient in dense phase of gelling agent	$D_{C,dense}$	1e-8cm <sup>2</sup> /s	Assumed
Diffusion coefficient in dilute phase of gelling agent	$D_{C,dilute}$	1e-6cm <sup>2</sup> /s	Assumed
Partition coefficient at cavity boundary	$P$	1	Assumed
Initial radius of tumor	$a$	0.5cm	[15]
Total dimension of simulation domain	$R$	2cm	Assumed

### 3.2.6 Obtaining Numerical Solution

To solve the continuum mechanics equations of tissue deformation (equations 8-14), we used Laplace transforms to obtain analytical expressions in the Laplace space and then used a numerical inverse Laplace transform solver in MATLAB. For the remaining equations, we used the finite difference numerical method. The spatial dimension was discretized to 1000 points, and the equations were converted to finite difference equations. More specifically, the backward difference method was used for equations at  $0 \leq r \leq r_c$ , and the central difference method was used for  $r_c < r \leq R$ ,

where  $R$  is the end of the simulation domain. This method was chosen to reduce stability concerns resulting from the moving boundary. Finally, the equations were solved using the stiff solver `ode15s` in MATLAB.

### ***3.3 Results and Discussion***

#### **3.3.1 Effect of Tissue Properties on Solid Deformation and Mass Transport**

Key outputs of our simulation include the pressure field, the velocity field, the solid displacement field, and the resulting cavity radius. The cavity radius and pressure field are particularly important because they may be tested experimentally. Our first goal was to study the effects of tissue properties, namely the hydraulic conductivity and tissue stiffness, on these outputs, and then analyze how that may ultimately affect API mass transport. Results show that a higher hydraulic conductivity leads to less solid deformation (Figure 9A), because the injected fluid can permeate into the tumor more readily. Consequently, smaller cavity radii are observed with higher hydraulic conductivities (Figure 9C). Similarly, because tumors with higher hydraulic conductivities are more permeable, we also observe faster transport of the API into and through tumor tissue. This results in reduced retention of the API within the cavity and tumor tissue over time (Figure 9D) and more permeation into the surrounding healthy tissue.

Lamé parameters are directly proportional to a material's Young's modulus. Higher values therefore correspond to a stiffer solid matrix, and this is reflected by reduced deformation (Figure 9B) and smaller cavity radii (Figure 9C). Interestingly, although the velocity field in tissue is independent of  $\mu$ , the concentration distribution of the API is affected by  $\mu$  (Figure 9H). This results in better retention of the API over time

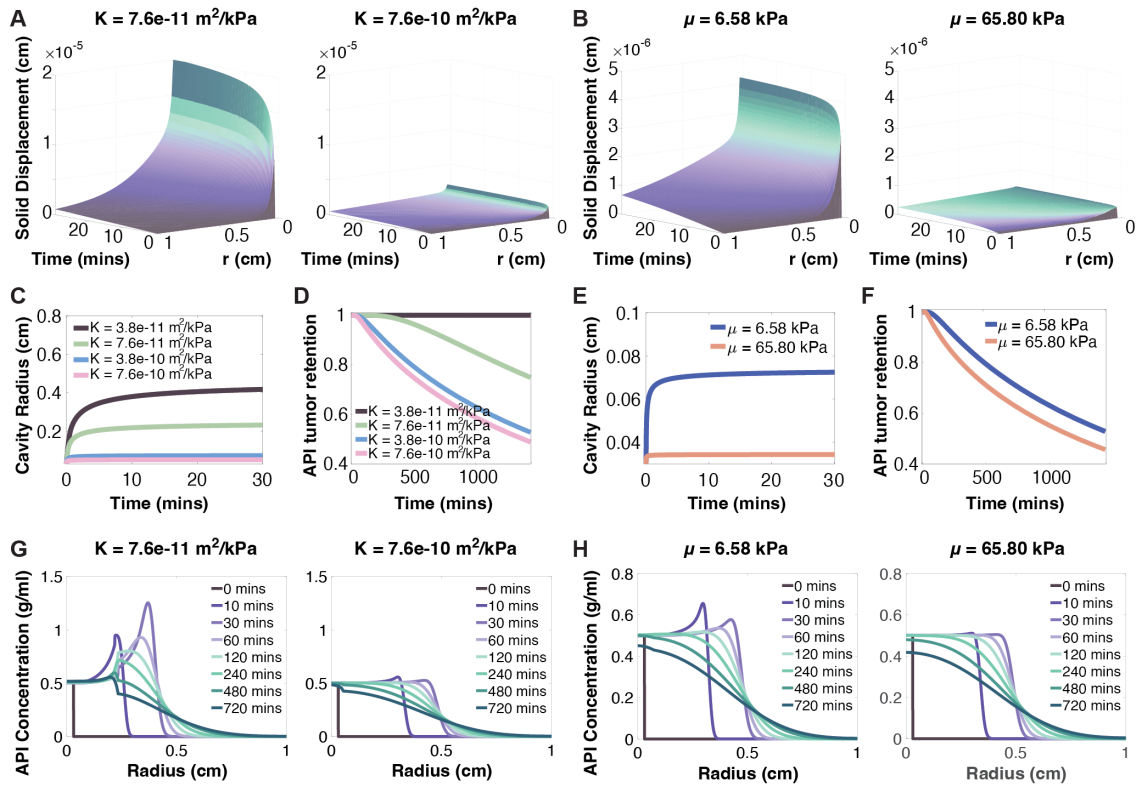


**Figure 9 Effect of varying hydraulic conductivity and tissue elasticity on cavity radius, and API mass transport**

**A** – Effect of varying hydraulic conductivities (left:  $K = 3.8 \times 10^{-11} \text{ m}^2/\text{kPa}$ , right:  $K = 7.6 \times 10^{-10} \text{ m}^2/\text{kPa}$ ) on solid displacement fields. Localized injections in tumors with higher hydraulic conductivities leads to smaller deformations. **B** – Effect of varying Lamé's second parameter  $\mu$  (left:  $\mu = 6.58 \text{ kPa}$ , right:  $\mu = 65.8 \text{ kPa}$ ) on solid displacement fields. Higher  $\mu$  tumors deform less. **C** – Cavity radius for different hydraulic conductivities. The cavity radius is calculated as the addition of the magnitude of the solid displacement field at  $r=r_0$  and  $r_0$ . **D** – Normalized fraction of API mass in cavity and tumor over time for different values of  $K$ . **E** – Cavity radius for different tissue elasticities. **F** – Normalized fraction of API mass in cavity and tumor over time for different values of  $\mu$ . **G** – Representative API concentration plots over radial distance at different time points, for different values of  $K$  – Representative API concentration plots over radial distance at different time points for different values of  $\mu$ .

inside softer, more elastic tumor tissue (Figure 9F). This may be due to the differences in the size of the cavity. In stiffer tissue, smaller cavity radii during the injection results in a smaller effective distance for transport, thus increasing the speed of API permeation through the tumor and causing less retention of the API within the tumor margins.

### 3.3.2 Effect of Injection Parameters on API Retention in Tumor Tissue

The volume injected and the flow rate are key injection parameters that greatly affect the efficacy of localized injections [10, 14]. Optimizing these parameters for specific tissue types is of great importance to effective therapies. Here, we study the effects of these two parameters on pressure, the velocity field, the cavity radius, and ultimately, the API concentration distribution. As a standard baseline, the model predicts that the pressure field increases in time and decreases over radius (Figure 10A), and that the velocity field follows the same trend (not shown). For simplicity, here we analyze the pressure and velocity over time at  $r=r_0$ , where we expect the magnitude of these outputs to have their highest value.

As expected, higher injection flow rates lead to elevated pressures, larger cavity radii and faster fluid velocities (Figure 10B). However, keeping volume injected constant, the injection phase is shorter, and so pressure and velocity are high for shorter time. This plays a key role in API mass transport, as high flow rates for shorter time periods exhibits significantly better retention of the API within the cavity and tumor tissue compared to lower flow rates (Figure 10D). One key limitation of this analysis, however, is the absence of tissue fracture in the model, which may indeed occur when the pressure on the surface of the cavity exceeds the critical pressure of tissue. Fracture of the solid tissue matrix would cause the formation of conduits for leakage. This is discussed further, below.

Although adding a gelling agent would help plug in these conduits, depending on the dynamics of phase separation relative to the rate of fracture formation, injections at higher flow rates might approach a point of diminishing returns and worse efficacy. A more complex model that accounts for tissue damage in the physics of mass transport

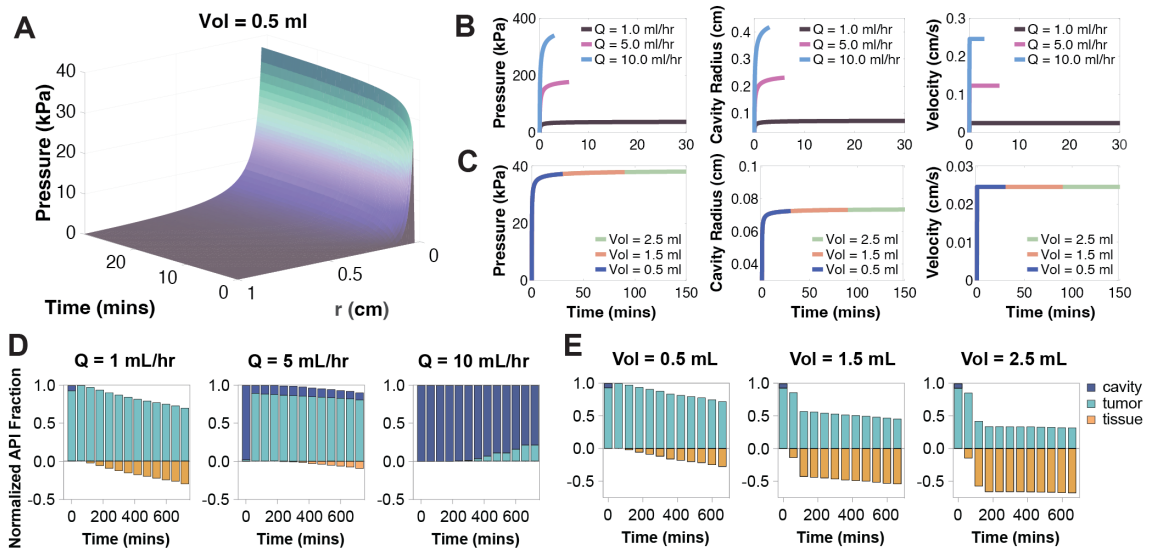


**Figure 10** Effect of injection parameters  $Q$  and  $V$  on pressure, cavity radius, fluid velocity and on final distribution of API within domain.

**A** – representative pressure field for an injection volume of 0.5mL. **B** – pressure, cavity radius, and fluid velocity over time for different injection flow rates. **C** – pressure, cavity radius and velocity over time for different injection volumes. **D** – normalized API distribution in cavity, tumor tissue and surrounding healthy tissue over time given different flow rates. The mass fraction in the cavity and tumor are positive, while that in the tissue is negative to show leakage out of the target delivery zone. **E** – same as **D**, but for varying injection volumes.

and tissue deformation mechanics may help explore and clarify some of these relationships.

The effects of volume on key injection outputs are slightly more nuanced. Given a constant flow rate, changing volume does not significantly affect the pressure, velocity, or final cavity radius (Figure 10C). However, because a higher injected volume results in a longer injection, the velocity field is non-zero for longer, giving more time for convection to progress. This results in lower retention of the API in the tumor (Figure 10E).

### **3.3.3 Precipitation Dynamics and Diffusion Coefficients have Small Effect on API Tumor Retention**

The mobility coefficient  $M$  affects the rate of phase separation in a biphasic mixture. Here, we analyzed ranging  $M$  values across 5 orders of magnitude, from  $3e-9$  to  $3e-13\text{cm}^2/\text{s}$ . Although results do show significant changes in the dynamics of phase separation across time (Figure 11A), mass transport outputs including API concentration profiles (Figure 11C) and the normalized mass distribution of the API across the cavity, tumor and surrounding healthy tissue (Figure 11B) remain largely unchanged. There are two critical factors that lead to this result. The first is the constant order boundary condition set on the Cahn Hilliard equation at the surface of the cavity, which assumes instantaneous phase separation of the sustained release gelling agent into its dense phase at the cavity boundary. Since the cavity grows over time, assuming instantaneous-precipitation at the moving interface results in the progressive formation

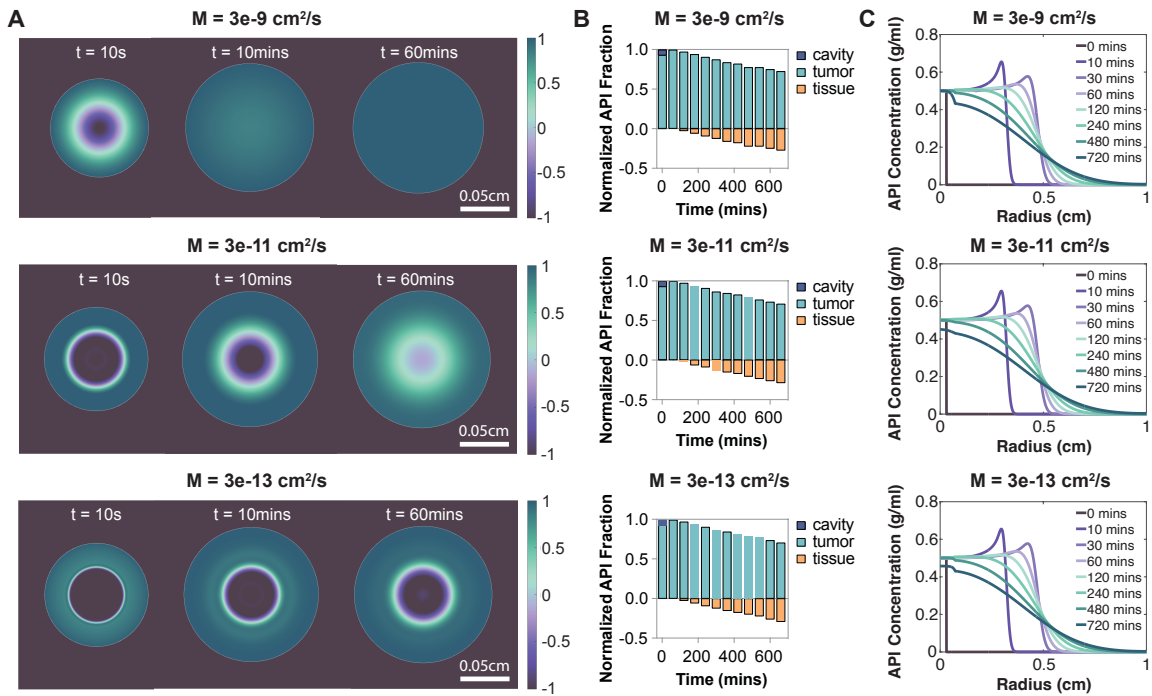


**Figure 11 Effect of mobility coefficient  $M$  on gelling agent precipitation dynamics and resulting API mass transport.**

**A** – Representative heatmaps of Cahn-Hilliard order parameter as a function of  $M$  10 seconds (left), 10 minutes (middle) and 60 minutes (right) since the start of the injection. A higher value of  $M$  leads to faster precipitation, so a higher distribution of dense phase within the cavity. The white edge shows the tumor-cavity boundary, as calculated from the continuum mechanics tissue deformation model. **B** – distribution of API in the cavity, tumor and tissue over time given varying values of  $M$ . **C** – Concentration of API over radius for different time points given different values of  $M$ .

of a shell of dense-phase precipitate that expands outwards as the cavity grows. This shell behaves as a barrier for diffusive transport. The shell becomes thick relative to the size of the cavity very rapidly due to the speed of cavity growth, which is significantly faster than the spontaneous rate of phase separation modulated by the mobility coefficient. Thus,  $M$  does not significantly impact shell formation, and consequently does not influence the net rate of diffusive transport through the shell. The second and more significant reason for the insensitivity of mass transport to the mobility coefficient is the dominance of convection during the injection phase (high Peclet number). In general,

fluid velocity increases rapidly at the onset of injection, and this high velocity is sustained during the entire course of the injection. As a result, the API is pushed quickly via convective transport out of the cavity and into the tumor tissue. Since we are assuming that the gelling agent is too large to permeate into the tumor, API mass transport continues unhindered within the tumor tissue and beyond, insensitive to the physicochemical processes occurring inside the cavity. By the beginning of the relaxation phase, when diffusion becomes dominant and the shell in the cavity finally plays a more important role in overall mass transport, there is only a small fraction of API left in the cavity to be contained by the dense-phase gelling agent.

This reasoning is further supported by the lack of sensitivity of the mass transport results to varying diffusion coefficients in the dense phase of the precipitate. Reducing the value of this parameter significantly impacts the concentration profiles at small values of  $r$ , in the cavity and its immediate surroundings in the tumor (Figures 12A,B).

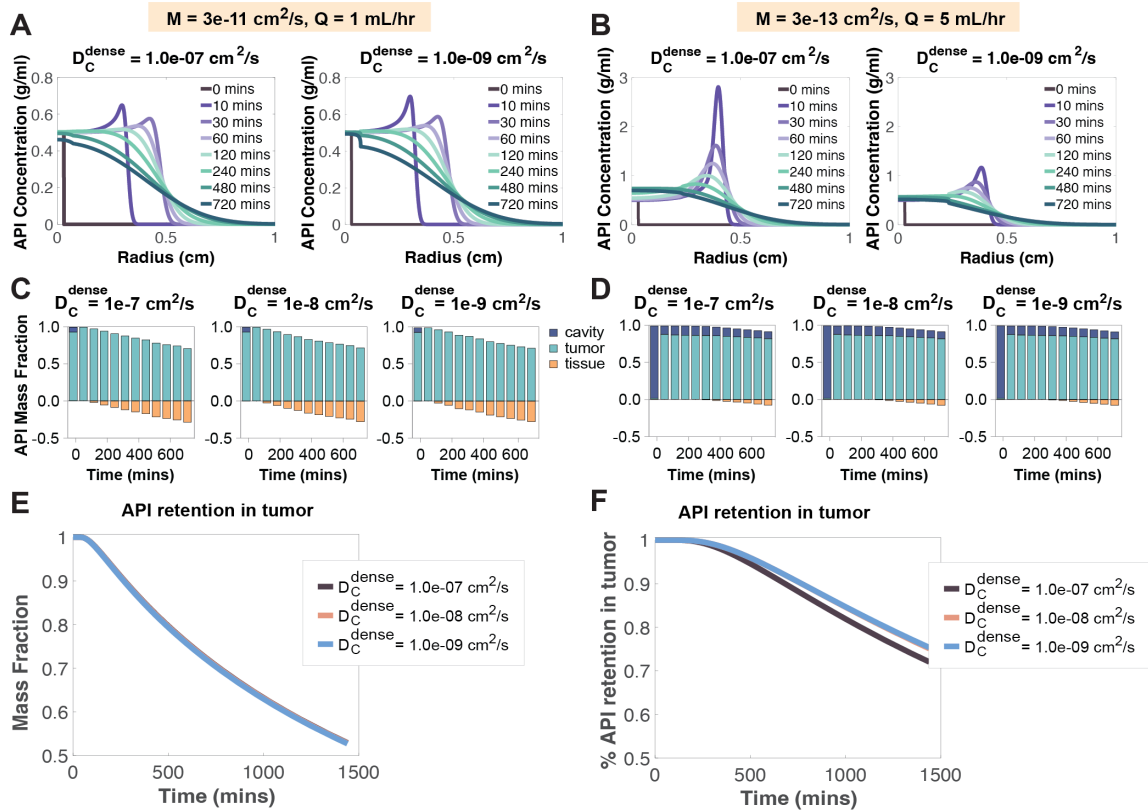


**Figure 12** Effect of varying the diffusion coefficient in the dense phase of the gelling agent on API mass transport.

**A** - API concentration profiles vs radial distance from center for different time points, given decreasing values of  $D_{C,dense}$ . Values of the mobility coefficient  $M$  and the flow rate  $Q$  are  $3e-11\text{cm}^2/\text{s}$  and  $1\text{mL/hr}$  respectively. **B** – Same as **A**, but for  $M = 3e-13\text{cm}^2/\text{s}$  and  $Q = 5\text{mL/hr}$ . **C** – Mass fraction of the API in the cavity, the tumor and in tissue. We show this fraction as negative in tissue to portray undesired loss out of the bounds of the target tumor tissue.  $M = 3e-11\text{cm}^2/\text{s}$ ,  $Q = 1\text{mL/hr}$ . **D** - Same as **C**, but for  $M = 3e-13\text{cm}^2/\text{s}$ ,  $Q = 5\text{mL/hr}$ . **E** – API Mass fraction in the cavity and tumor over the span of 1 day.  $M = 3e-11\text{cm}^2/\text{s}$ ,  $Q = 1\text{mL/hr}$ . **F** - Same as **A**, but for  $M = 3e-13\text{cm}^2/\text{s}$ ,  $Q = 5\text{mL/hr}$ .

However, as  $r$  increases, the concentration profiles begin to converge. At the tumor-healthy tissue boundary and above ( $r \geq 0.5\text{cm}$ ), any differences in these profiles become effectively negligible. This phenomenon is exacerbated by the dominance of convection during the injection process, which results in the rapid increase of the API mass fraction in the tumor and a rapid depletion in the cavity. Since we assume that the sustained

release agent is too large to permeate into the tumor, once the API reaches the tumor, the agent can no longer affect its transport. As a result, the mass fractions of the API in the cavity, the tumor and the tissue over time are the same regardless of the diffusion coefficient in the dense phase of the sustained-release agent (Figures 12C,E). One caveat to this observation is that if we increase the flow rate such that the cavity grows larger, this effectively reduces the distance between the cavity boundary and the tumor boundary, and so variations in the diffusion coefficient of the API start to become more important. Further, if the phase separation process is slowed down by reducing the mobility coefficient  $M$ , more nuance and variation are added to the heterogeneity of the phase continuum which also increases the sensitivity of the API's PK to the diffusion coefficient. This results in marginally improved API mass retention in the tumor for lower diffusion coefficients under these conditions (Figure 12D,F).

### **3.3.4 Model Limitations**

Our model introduces a valuable way of exploring localized injection of an API and a gelling agent; but simplifying assumptions were made in the construction of this model that might impose limitations depending on the application. One such assumption is that the gelling agent is too large to permeate into tumor tissue, so that it remains confined within the cavity. Although this assumption is reasonable given that common gelling agents are high molecular weight polymers, it is possible that during the injection phase, where convection is dominant, the pressure is high enough to push the dilute phase gelling agent through the porous tumor matrix. Similarly, the assumption of instantaneous precipitation of the gelling agent at the cavity boundary should be relaxed for increased accuracy. Prescribing a flux boundary condition that allows for transport of the gelling agent into the tumor during the injection, convection-dominant phase may be

a more appropriate assumption at the moving cavity boundary. These two changes would likely increase the sensitivity of mass transport outputs to the mobility coefficient  $M$  and the diffusion coefficient in the dense phase of the precipitate  $D_{C,dense}$ .

Another simplifying hypothesis is that of a constant, homogenous hydraulic conductivity throughout the tumor. Many studies have shown that  $K$  is sensitive to solid deformation and have used empirical equations to characterize  $K$  as a function of the dilatation or the strain tensor [93]. In our case, we are assuming a localized injection into tumor tissue, which tends to be stiff relative to healthy tissue. For small deformations relative to the size of the simulation domain, as would happen in stiff tissue, we can apply infinitesimal strain theory which allows us to impose constant parameters in the tumor, including the hydraulic conductivity and the diffusion coefficient of the API in tissue. However, applying a dilatation-dependent  $K$  may be more appropriate to model injections in softer tissues.

Our analysis of continuum solid displacement also assumes that tissue is a biphasic medium consisting of a poroelastic solid matrix and a fluid phase. In reality, tissue behaves more as a visco-poroelastic medium. However, prior studies have shown that including a viscous term in the solid stress relationship (equation 5) only affects the transient buildup of pressure and velocity, but at longer values of time dependence to this viscous term disappears [18] As such, we decided that for our analysis, this term was not necessary.

In the transition from the injection phase to the relaxation phase, we also assume that the cavity radius remains constant at its final size, and that the pressure and fluid velocity instantly drop to 0. This logic assumes that the time associated with the pressure and velocity drop at the end of the injection is negligible relative to the duration

of the injection phase. Further, our model neglects the effects of the phase separation process on pressure build up and fluid velocity. This is based on observations of ethyl cellulose (EC) injections, where EC rapidly precipitates out in water to form a soft, highly deformable precipitate [10]. Since the precipitate is so soft and easily displaced, we assume its contribution to both pressure and velocity to be negligible. However, for injections of phase-separating materials that form more rigid gels, this assumption should be re-evaluated. This dependence of pressure and velocity on gelling agent phase separation would enforce two-way coupling between the Cahn-Hilliard equations and the solid tumor tissue deformation mechanics.

Finally, here we use a simplified geometry that allows us to solve the system of equations in 1D spherical coordinates. These simplifications are motivated by observations that injection distribution volumes in rat liver are approximately spherical [13]. However, many superficial tumors are not spherical, and tissue properties in tumors and healthy tissue may be highly heterogenous and anisotropic, leading to non-spherical injectate distribution volumes. Accounting for this heterogeneity would be beneficial in modeling, especially for tumors with necrotic cores, which may have vastly anisotropic properties [98]. Our model also does not account for fracture of the solid tissue matrix, which may occur at high pressures. Incorporating a mathematical framework for tissue damage would be advantageous since it would provide a way of exploring API retention within the tumor due to plugging of tissue fractures by dense-phase gelling agents. However, such a model would be exponentially more complex. The model we present here is a foundational starting point, from which more complex mathematical formulations can be built.

### **3.4 Conclusions**

The model presented here is a framework to aid optimization of localized injections of therapeutics into tumors. Using Cahn-Hilliard theory, we integrate phase separation of a co-injected phase-separating agent to a mathematical framework of coupled biphasic, poroelastic tissue deformation and mass transport theory. This allows us to explore the dependence of key outputs, such as pressure, solid deformation, and API concentration profiles, on a complex set of parameters. These parameters include tissue-specific properties, API-specific mass transport parameters, injection-dependent parameters, and properties of the sustained release agent and its phase separation dynamics. The model is successful in capturing fundamental injection behaviors, including the dependence of solid deformation on hydraulic conductivity and tissue elasticity, and the formation of a shell of dense-phase gel at the cavity interface due to the dynamics of the phase separation process. Further, it reveals interesting findings such as improved API tumor retention for injections in softer, more elastic tumor tissues relative to stiffer tissues. However, the model also emphasizes the dependence of API mass transport on convection compared to diffusion. This dependency limits the impact of the sustained release agent's phase-separating dynamics on containment of the API within the bounds of the tumor, at least in the absence of fracture. It is possible that gelling agents may, to a large degree, improve API retention within the tumor by occluding conduits with low resistance to flow, such as blood vessels or regions damaged by the high injection pressures. However, exploration of these phenomena would require more complex models that implement fracture dynamics.

### 3.4.1 Application to Ethanol-Ethyl Cellulose Injections

The model presented above is a generalized tool that can be utilized to optimize ethanol-ethyl cellulose injections for various tissue types in the absence of tissue fracture. However, there remain some unknown factors and effects that need to be incorporated before the model can be best applied to our application of interest. We elaborate on these unknowns below and provide strategies to uncover them.

1. The nature of the mobility coefficient (the rate of phase separation) and its relationship to ethyl cellulose concentration is currently unclear. In our analysis, we are assuming this parameter to be constant. However, it can also be an empirical function of temperature or pH, for instance, if the gelling agent is sensitive to these. In the case of ethyl cellulose, it may depend on the mass fraction of ethyl cellulose relative to water and ethanol. One potential approach to learn more about this parameter is to perform injections of ethanol-ethyl cellulose into pure water and observe the speed of phase separation. Measuring the radius of the cloud formed by the dense-phase ethyl cellulose over time would be a first pass approach to determine if the mobility coefficient is constant or if it changes over time. This same experiment could be performed for injections into surrogates of different concentrations (i.e., different water mass fractions), to analyze how sensitive the phase separation process is to water content and to the relative ethyl cellulose concentration. From a quantitative perspective this experiment would also be valuable in obtaining estimates for the mobility coefficient given different water contents.

One potential difficulty in running these experiments is the polydispersity of ethyl cellulose, which adds considerable variability. Using a surrogate sustained-release

agent with a similar molecular weight and a much tighter polydispersity index be beneficial to reduce variability and get a better understanding of the mobility coefficient in a better controlled environment.

2. These same experiments suggested in 1. may help reveal insights into the boundary condition to the Cahn-Hilliard equation at the radius of the cavity,  $r = r_c$ . In our framework, we assumed a constant concentration boundary condition for the order parameter at the boundary with the tumor, which assumes instantaneous precipitation of ethyl cellulose when in contact with the aqueous environment. Although this boundary condition seemed appropriate given observations of rapid ethyl cellulose precipitation in water, results of the model suggest that this reduced the sensitivity of the concentration profiles to the mobility coefficient and the diffusion coefficient of ethanol in the dense phase. It is currently unclear if assuming instantaneous precipitation at the boundary is an assumption that should be relaxed into a more nuanced relationship. The experiments proposed in 1. would deliver more insight into this unknown. For example, if we find that the mobility coefficient does depend on ethyl cellulose concentration, then a Neumann, flux boundary condition may be more appropriate.
3. The next unknown is the relationship between the diffusion coefficient in the dense-phase material and the concentration of ethyl cellulose. Here, we assume this relationship to be linear. However, non-linearities might significantly increase the sensitivity of ethanol transport to the dynamics of phase separation. Further, the diffusion coefficient of ethanol in the liquid phase also needs to be estimated as an input to the model. These unknowns can be measured via Franz-cell experiments, allowing us to estimate the diffusion of ethanol through mixtures with different

concentrations of ethyl cellulose in water and ethyl cellulose in ethanol. If this experiment is performed such that measurements are taken using Raman spectroscopy, or some other kind of real-time, label-free measurement system, it is possible to compute the partition coefficient of ethanol at the cavity-tumor interface as well. The partition coefficient can be estimated as the ratio of the solubilities of the API in the two compartments. Here, this value is assumed as unity for simplicity. However, future studies should use a value that appropriately represents the relative solubilities of their chosen API in tumor tissue and in the dense, phase-separated, co-injected material.

Once these questions are answered, the next step is to apply the model with all updated parameters and relationships. More specifically, given an initial ethyl cellulose concentration, we should apply the corresponding diffusion coefficients of ethanol in the dense and dilute phases of ethyl cellulose. These updated variables would be plugged into a revised version of equation 44, modified if the experiments revealed non-linear behaviors. The corresponding mobility coefficient should also be modified accordingly. If it turns out that this coefficient is a function of ethyl cellulose concentration, then the convection-diffusion equation (equation 49) would need to be adjusted to account for that. Finally, the boundary condition at the cavity-tumor boundary would also need to be updated. With this, the inputs of the model would be completely defined, including those that depend on the initial ethyl cellulose concentration.

Key outputs from the model that could be tested include the pressure inside the cavity, which we could compare with injection pressure measurements, the radius of the cavity, which we may obtain by sectioning injected tumors at specified time points, and

the volume of the ethanol cloud, currently measured via CT, which we can predict with our model as well.

After testing, the model can be used to inform future injections in several tissue types, which are characterized by different Lamé parameters and hydraulic conductivities to ethanol. In this process, one key parameter is the pressure in the cavity, which is an output of the model. If the pressure is greater than the critical pressure of tissue, then we know that tissue fracture may occur. Thus, although the model presented here does not mathematically account for fracture, it may predict a possibility of fracture, helping us interpret experimental results in that light and providing benchmarks to avoid it. In situations when fracture does not occur, then the model becomes directly applicable. By performing a sensitivity analysis and analyzing the relationships between the various input parameters, it is possible to, given tissue-specific constraints, maximize output metrics such as ethanol retention inside the tumor given input injection parameters.

### **3.4.2 Implications for Injections in Different Tissue Types**

Applications of interest for intratumoral injections of ethanol-ethyl cellulose include treatment of cervical dysplasia and cervical cancer, breast cancer tumor ablation, and hepatocellular carcinoma ablation. As per our analysis in section 3.3.1, differing tissue properties, including tissue stiffness and hydraulic conductivity, may greatly affect injection efficacy in the absence and presence of a phase-separating material. Use of our model to perform quantitative, tissue-specific predictions of injection efficacy would require in-depth material characterization studies to obtain tissue-specific parameters. However, some qualitative insights about injection efficacy can be obtained based on prior characterization work in the literature and results from our analysis. In

this section, we briefly review what is known about tissue stiffness (as measured by the Young's modulus) and hydraulic conductivity in hepatocellular carcinomas, cervical carcinomas, and breast tumors. Then, we discuss how our model, in the context of this body of knowledge, may help guide interpretation of injection efficacy in these three tissue types.

The mean Elastic moduli of healthy breast tissue, liver tissue and cervical tissue have been estimated in the ranges of 0.4-5kPa, 1-10kPa and 15-50kPa respectively [99-104]. These values are sensitive to a plethora of parameters and processes, including fat content, inflammation, natural tissue heterogeneity, and even the characteristics of the measurement protocol itself [99, 105-107]. Further, pregnancy may also influence tissue stiffness in breast tissue and cervical tissue [102] and fibrosis and other liver pathologies may also affect liver tissue stiffness [101]. These various confounding factors contribute to the highly variable and heterogenous nature of the Young's modulus.

Prior work suggests that although tumor cells tend to be softer than healthy cells, solid tumors tend to have a more collagen-rich extracellular matrix. This generally leads to increased stiffness and higher Elastic moduli in solid tumors relative to their healthy counterparts [108, 109]. The average elastic modulus of breast cancer tumors has been measured in the range of 10-42kPa [104, 107], hepatocellular carcinoma in the range of 25-35kPa [101, 110, 111], and cervical tumors in the range of 30-90kPa [112]. Like in healthy tissue, there is a large degree of variability associated with these measurements, which is exacerbated by the heterogeneity of tumor tissue that may contain necrotic cores, and by the variability between tumor types and cancer stage.

The hydraulic conductivity of tissue is also highly heterogenous, and it greatly affects the rate of convective drug transport [113]. Studies have shown that the hydraulic conductivity follows an inverse relationship with collagen fiber density and glycosaminoglycan (GAG) content in many tumor types [113, 114]. As a result, solid tumors with collagen-rich extracellular matrices tend to have significantly lower hydraulic conductivities relative to their healthy counterparts [113]. Some sources estimate the hydraulic conductivity in various tumors to be in the range of  $10^{-15}$ - $10^{-13}$  m<sup>2</sup>/Pa·s [113], with cervical and hepatocellular carcinomas generally towards the higher end of this range [115, 116] and breast tumors towards the middle [117].

Our model estimates that localized injections in softer, less stiff tissues, and in tissues with lower hydraulic conductivities, exhibit superior API retention within the bounds of the target region (Figure 9). In general, solid tumors with collagen-rich extracellular matrices tend to be less permeable, but also stiffer. Therefore, in these solid tumors there is a competing effect between stiffness and hydraulic conductivity which makes it difficult to make generalizable assertions about API retention and injection efficacy. In the context of our tissue types of interest, breast tumor tissue tends to be both softer and less permeable on average compared to hepatocellular carcinomas and cervical tumors, liver tissue is also soft but has a higher hydraulic conductivity, and cervical tissue is both stiff and has a high hydraulic conductivity. This suggests that intratumoral injections may exhibit superior API retention in breast tumors, followed by hepatocellular carcinomas, and lower retention in cervical tumors. However, given the large number of confounding variables and the high heterogeneity and variability in these parameters, it is problematic to make generalizable assertions, and it is more appropriate to apply our interpretations in quantitative patient-specific and/or tissue-

specific manners. With the mathematical framework presented in this work, making such analyses is simple and quick, as it only requires changing the values of these parameters.

Our intratumoral injection model does not account for tissue fracture since this would make our analysis significantly more complex. Nonetheless, fracture is a key mechanism that contributes to API leakage and lower ablation efficacy. Therefore, another parameter that we should keep in mind is the ultimate compressive strength of tissue. This is important because tissues with a higher compressive strength may be more robust and require a higher critical pressure to fracture. Physical plugging of fractures and damaged regions by phase-separated ethyl cellulose may help reduce leakage and the sensitivity of API retention on the ultimate compressive strength of tissue. Further material characterization and injection experiments, both *ex vivo* and *in vivo*, are needed to characterize the compressive strength of target tissues and to understand the impact of ethyl cellulose on reducing API leakage via fractures.

## 4. Conclusion and Future Directions

The work presented in this dissertation explores the value of top-down, deterministic mathematical models in characterizing drug delivery problems for women's health applications. We investigated two projects: 1. A mathematical model that computes the probability of infection in women after sexual exposure to HIV by coupling HIV transport, anti-HIV microbicide drug transport and viral dynamics in the female reproductive tract and in blood; and 2. A deterministic mathematical model of intratumoral injection that includes poroelastic tissue deformation and phase separation of a co-injected sustained release agent that solidifies in tissue. Our approach for both projects was mechanistic and systematic. We identified key phenomena involved each problem, built mechanistic models for each of these processes and tested their outputs, and finally we coupled everything together into a unified mathematical framework. Our models are based on deterministic physical laws and conservation principles applied to our problem, simplified when appropriate, and solved numerically. At each iteration in this process, we tested our models for several parameter values and interpreted the results to ensure that the correct physics was captured.

Our main objective for the POI project was to develop a standardized PD metric that could be used to compare the efficacy of topically applied anti-HIV microbicide products under various circumstances, such as different drug administration conditions. This is motivated by the experimental difficulty in testing new microbicide product candidates *in vitro* and *in vivo* in ways that properly represent real world use. This issue is exacerbated by the lack of PD testing standardization between drug candidates, which also contributes to the inefficiencies of current anti-HIV drug development. With the POI model, we aimed to build a tool that would help evaluate performance under different

circumstances and inform future microbicide design. In doing so, it was necessary to construct a system that accounted for spatiotemporal heterogeneity as it relates to transport and the dynamics of infection, as the nuances of the distribution of drug relative to that of the virus in the female reproductive tract is important to the outcome of infection. For instance, if the timing of drug administration is too early relative to the time of exposure, drug clearance may result in reduced protection. The POI model we built is deterministic in nature, so to compute the POI and to account for inter-user variability, we used the Monte Carlo method. This involved generating distributions of parameters relevant to the anatomy of the female reproductive tract and the dynamics of infection, and sampling from those distributions to simulate a population of susceptible women exposed to HIV.

The model revealed interesting insights regarding the circumstances of infection. For example, results show that infection may occur first in vaginal tissue, or in the blood stream. The latter happens frequently with the chosen parameters due to the initial density of infectible cells in the blood, which is significantly higher than that in vaginal tissue. This is particularly true if the transfer rate from the stroma to the bloodstream is high. In these circumstances, administration of an anti-HIV microbicide like TFV, which we tested here, would not provide effective protection. Our analysis of infection at different stages during the menstrual cycle further emphasized the sensitivity of infection to the infectible cell density, with the POI being significantly higher during the luteal phase due largely to a higher cell density in vaginal tissue.

Despite the models' accurate characterization of important phenomena and valuable predictions of anti-HIV protection, it also has several limitations. Perhaps the most important one is that it does not account for infection propagation in lymph nodes

or the possibility of acute infection in the cervix, both of which occur frequently during sexual HIV exposure. Further, more tests should be performed to evaluate the ability of the model to successfully compute the POI for different microbicide delivery modes, including intravaginal rings and dissolving inserts. Despite the increased complexity, further development may not only enhance the model's accuracy, but also its versatility and utility in rational drug design.

The intratumoral injection modeling project was motivated mainly by intratumoral injections of ethanol and the water-insoluble polymer ethyl cellulose, which have shown promise as a low-cost tumor ablation alternative [10-15, 118, 119]. Initially, the target of choice for this new therapy was cervical cancer, but applications in liver and breast tumor ablation are also being investigated. One difficulty in optimizing the injection procedure is the vast parameter space that is difficult to explore experimentally, given that experiments only provide snapshots into the process. A mathematical model of this process would allow us to view the relationships between input injection parameters and drug PK as a continuum. However, a significant limitation of current models in the literature is the lack of a theoretical framework that includes phase separation behavior of a co-injected gelling agent. Our goal was to build a tool that outlined the fundamental physics governing the injection process and includes phase separation dynamics of a co-injected as well. For that purpose, we integrated Cahn-Hilliard theory to a biphasic tissue deformation model. Further, we incorporated mass transport convection-diffusion theory as a function of the phase outputted by the Cahn-Hilliard mathematical formulation.

The ethanol injection model successfully identifies and elaborates important valuable phenomena, including for example the formation of a shell of phase-separated

material at the bound of the growing injection cavity. Further, it also successfully characterizes expected behavior, such as larger cavity grow due to reduced tissue hydraulic conductivities or higher tissue elasticity. However, the model also revealed an insensitivity of drug PK to important parameters including the mobility coefficient and the diffusion coefficient in the dense phase of the co-injected sustained release agent. These results emphasized the dominance of convection during the injection process and revealed some limitations in the assumptions made for our boundary conditions. Indeed, instantaneous phase-separation when in contact with tumor tissue is a simplifying assumption that may need to be addressed for improved accuracy.

#### ***4.1 Future Directions***

From a development point of view, the clear next step for the POI project is to do more extensive testing. This includes a deeper exploration into parameter space via a rigorous sensitivity analysis, which would further uncover the strengths and limitations of the model and allow us to identify and address inappropriate assumptions. Further, this would allow us to identify the parameters and processes that play the biggest role in the infection process. Following that, we would assess the feasibility of increasing accuracy by incorporating transport to lymph nodes and infection in the cervix, which are influential to the propagation of infection. However, incorporating these phenomena would increase complexity and in the best-case scenario cause a greater overestimation of the POI, so its value to the model's accuracy should be evaluated carefully.

Ultimately, the objective of this project was to evaluate and compare the efficacy of different microbicide products. Therefore, from an application perspective, the next step is to test the model for different anti-HIV drugs and delivery formulations. As part of

this analysis, it would be interesting to conduct four studies: 1. Comparisons between existing products for which we have a lot of PK and efficacy data; 2. Comparisons between different intravaginal topical drug delivery modes for the same drug; 3. Comparisons between different drugs administered using the same delivery method; 4. Analyses of current promising drug candidates. For 1, one interesting test would be to compare the TFV gel with dapivirine-releasing intravaginal rings. As a product that is heavily utilized, clinical data on the IVR ring is plentiful [21-23], and this analysis would also enable comparisons between the forgiveness of these products to improper user adherence. For study 2, focusing on the drug dapivirine would allow us to compare gels, films, and rings, all of which have been clinically tested for PK measurements, efficacy, and safety [21, 120]. Although experiments suggest that gels and films exhibit similar drug PK profiles [120], our model would enable more nuanced comparisons under different administration conditions, and potentially reveal some benefits and disadvantages of using one drug delivery mode over another. For analysis 3, it would be interesting to compare different classes of drugs, for example, entry inhibitors vs. NRTIs, NNRTIs or PIs, to obtain a better understanding of how the various mechanisms of action in their relation to dosing conditions affect the POI. Finally, for study 4, modifying the code to enable analysis of monoclonal antibody delivery would be particularly exciting, as it would allow us to evaluate a newer type of anti-HIV drug prevention method that has shown significant promise [121-123], and compare it to classical small molecule drugs.

Although the intratumoral injection model was initially motivated by the ethanol-ethyl cellulose injections, for robustness and generality we built a more abstract model that was applicable to injections of any API and gelling or phase-separating sustained

release agent. In doing so, we created a powerful theoretical framework, and our next step is to begin using the model for its intended application; optimization of ethanol intratumoral injections intended to ablate the tumors. This may include delivery of ethanol alone, or simultaneous delivery of a drug cocktail including ethanol and several chemotherapeutic molecules. The first step in this process is to test our conceptualization of phase separation more rigorously, by simplifying our model for injections into water, and directly comparing our predictions to experimental measurements of ethyl cellulose injections. This would allow us to assess the boundary condition imposed in the model at the interface between the injected ethyl cellulose and the surrounding aqueous environment. It would also give an opportunity to estimate ranges for the mobility coefficient. Stepping up this analysis, experimental injections of ethyl cellulose into hydrated tissue would be the next step building up to iterative optimization of our boundary conditions and mobility coefficient estimations. Further parameter estimations, for example, of the diffusion coefficient of ethanol in the dense and liquid phases of ethyl cellulose, are also required to make our model more translatable. Importantly, many of these parameters may depend on the initial concentration of ethyl cellulose in the injectate. Understanding the relationships between initial ethyl cellulose concentration and injectate viscosity, diffusion coefficients in the liquid and dense phase, and hydraulic conductivity are all imperative to achieve our goal of directly applying our model to optimize ethanol ablation injections. It is also important to remember that fracture and leakage are occur frequently during intratumoral injections due to high injection pressures. In the future we should explore options to incorporate simplified conceptualization of these mechanisms to assess the impact of a phase-

separating agent on drug PK in the presence and absence of tissue damage and fracture.

## References

1. Kaitin, K.I., *Deconstructing the drug development process: the new face of innovation*. Clin Pharmacol Ther, 2010. **87**(3): p. 356-61.
2. Duwal, S. and M. von Kleist, *Top-down and bottom-up modeling in system pharmacology to understand clinical efficacy: An example with NRTIs of HIV-1*. Eur J Pharm Sci, 2016. **94**: p. 72-83.
3. Jones, H. and K. Rowland-Yeo, *Basic concepts in physiologically based pharmacokinetic modeling in drug discovery and development*. CPT Pharmacometrics Syst Pharmacol, 2013. **2**(8): p. e63.
4. Lagenaur, L.A.B., E. A., *An anti-HIV microbicide comes alive*. Proc Natl Acad Sci U S A, 2005. **102**(35).
5. Ramjee, G., A. Kamali, and S. McCormack, *The last decade of microbicide clinical trials in Africa: from hypothesis to facts*. AIDS, 2010. **24 Suppl 4**: p. S40-9.
6. Celum, C. and J.M. Baeten, *Tenofovir-based pre-exposure prophylaxis for HIV prevention: evolving evidence*. Curr Opin Infect Dis, 2012. **25**(1): p. 51-7.
7. Abdool Karim, S.S., C. Baxter, and Q. Abdool Karim, *Advancing HIV prevention using tenofovir-based pre-exposure prophylaxis*. Antivir Ther, 2022. **27**(2): p. 13596535211067589.
8. Murewanhema, G., M. Malisheni, and N.F. Takah, *The effectiveness of tenofovir-based pre-exposure prophylaxis for prevention of HIV acquisition among sub-Saharan African women at high risk: a systematic review*. Pan Afr Med J, 2021. **38**: p. 308.
9. Coelho, L.E., et al., *Pre-exposure prophylaxis 2.0: new drugs and technologies in the pipeline*. Lancet HIV, 2019. **6**(11): p. e788-e799.
10. Morhard, R., et al., *Development of enhanced ethanol ablation as an alternative to surgery in treatment of superficial solid tumors*. Sci Rep, 2017. **7**(1): p. 8750.
11. Nief, C.A., et al., *Ethanol Ablation Therapy Drives Immune-Mediated Antitumor Effects in Murine Breast Cancer Models*. Cancers (Basel), 2022. **14**(19).
12. Mueller, J.L., et al., *Optimizing ethyl cellulose-ethanol delivery towards enabling ablation of cervical dysplasia*. Sci Rep, 2021. **11**(1): p. 16869.

13. Chelales, E., et al., *Radiologic-pathologic analysis of increased ethanol localization and ablative extent achieved by ethyl cellulose*. Sci Rep, 2021. **11**(1): p. 20700.
14. Morhard, R., et al., *Understanding Factors Governing Distribution Volume of Ethyl Cellulose-Ethanol to Optimize Ablative Therapy in the Liver*. IEEE Trans Biomed Eng, 2020. **67**(8): p. 2337-2348.
15. Nief, C., et al., *Polymer-assisted intratumoral delivery of ethanol: Preclinical investigation of safety and efficacy in a murine breast cancer model*. PLoS One, 2021. **16**(1): p. e0234535.
16. Ateshian, G.A., et al., *Finite deformation biphasic material properties of bovine articular cartilage from confined compression experiments*. J Biomech, 1997. **30**(11-12): p. 1157-64.
17. Netti, P.A.B., L.T.; Boucher, Y. , *Macro- and Microscopic Fluid Transport in Living Tissues: Application to Solid Tumors*. AIChE Journal, 1997. **43**(3).
18. Netti, P.A.T., F.; Jain, R.K., *Coupled Macromolecular Transport and Gel Mechanics: Poroviscoelastic Approach*. AIChE Journal, 2003. **49**(6): p. 1580-1596.
19. E, O.M., et al., *Oral pre-exposure prophylaxis (PrEP) to prevent HIV: a systematic review and meta-analysis of clinical effectiveness, safety, adherence and risk compensation in all populations*. BMJ Open, 2022. **12**(5): p. e048478.
20. Cambou, M.C. and R.J. Landovitz, *Challenges and Opportunities for Preexposure Prophylaxis*. Top Antivir Med, 2021. **29**(4): p. 399-406.
21. Nel, A., et al., *Safety and Efficacy of a Dapivirine Vaginal Ring for HIV Prevention in Women*. N Engl J Med, 2016. **375**(22): p. 2133-2143.
22. Baeten, J.M., et al., *Use of a Vaginal Ring Containing Dapivirine for HIV-1 Prevention in Women*. N Engl J Med, 2016. **375**(22): p. 2121-2132.
23. Bhavaraju, N., et al., *Introducing the Dapivirine Vaginal Ring in Sub-Saharan Africa: What Can We Learn from Oral PrEP?* Curr HIV/AIDS Rep, 2021. **18**(6): p. 508-517.
24. Molina, J.M., et al., *Challenges and opportunities for oral pre-exposure prophylaxis in the prevention of HIV infection: where are we in Europe?* BMC Med, 2013. **11**: p. 186.

25. Parikh, U.M., et al., *Complete protection from repeated vaginal simian-human immunodeficiency virus exposures in macaques by a topical gel containing tenofovir alone or with emtricitabine*. J Virol, 2009. **83**(20): p. 10358-65.
26. Vanpouille, C., A. Arakelyan, and L. Margolis, *Microbicides: still a long road to success*. Trends Microbiol, 2012. **20**(8): p. 369-75.
27. Gorbach, P.M., et al., *Effects of partnership change on microbicide gel adherence in a clinical trial (HPTN 035)*. AIDS Behav, 2014. **18**(5): p. 855-61.
28. Gao, Y. and D.F. Katz, *Multicompartmental pharmacokinetic model of tenofovir delivery by a vaginal gel*. PLoS One, 2013. **8**(9): p. e74404.
29. Gao, Y., et al., *Vaginal deployment and tenofovir delivery by microbicide gels*. Drug Deliv Transl Res, 2015. **5**(3): p. 279-94.
30. Katz, D.F., A. Yuan, and Y. Gao, *Vaginal drug distribution modeling*. Adv Drug Deliv Rev, 2015. **92**: p. 2-13.
31. Kearney, B.P., J.F. Flaherty, and J. Shah, *Tenofovir disoproxil fumarate: clinical pharmacology and pharmacokinetics*. Clin Pharmacokinet, 2004. **43**(9): p. 595-612.
32. Barditch-Crovo, P., et al., *Phase i/ii trial of the pharmacokinetics, safety, and antiretroviral activity of tenofovir disoproxil fumarate in human immunodeficiency virus-infected adults*. Antimicrob Agents Chemother, 2001. **45**(10): p. 2733-9.
33. Hendrix, C.W., et al., *MTN-001: randomized pharmacokinetic cross-over study comparing tenofovir vaginal gel and oral tablets in vaginal tissue and other compartments*. PLoS One, 2013. **8**(1): p. e55013.
34. Stafford, M.A., et al., *Modeling plasma virus concentration during primary HIV infection*. J Theor Biol, 2000. **203**(3): p. 285-301.
35. Rong, L. and A.S. Perelson, *Modeling latently infected cell activation: viral and latent reservoir persistence, and viral blips in HIV-infected patients on potent therapy*. PLoS Comput Biol, 2009. **5**(10): p. e1000533.
36. Hill, A.L., *Mathematical Models of HIV Latency*. Curr Top Microbiol Immunol, 2018. **417**: p. 131-156.
37. Perelson, A.S., *Modelling viral and immune system dynamics*. Nat Rev Immunol, 2002. **2**(1): p. 28-36.

38. Perelson, A.S. and R.M. Ribeiro, *Modeling the within-host dynamics of HIV infection*. BMC Biol, 2013. **11**: p. 96.
39. Graw, F. and A.S. Perelson, *Modeling Viral Spread*. Annu Rev Virol, 2016. **3**(1): p. 555-572.
40. Garcia-Cremades, M., et al., *Modeling the Probability of HIV Infection over Time in High-Risk Seronegative Participants Receiving Placebo in Five Randomized Double-Blind Placebo-Controlled HIV Pre-Exposure Prophylaxis Trials: A Patient-Level Pooled Analysis*. Pharmaceutics, 2022. **14**(9).
41. Tuckwell, H.C., P.D. Shipman, and A.S. Perelson, *The probability of HIV infection in a new host and its reduction with microbicides*. Math Biosci, 2008. **214**(1-2): p. 81-6.
42. Bonhoeffer, S., et al., *Virus dynamics and drug therapy*. Proc Natl Acad Sci U S A, 1997. **94**(13): p. 6971-6.
43. Naranbhai, V., et al., *Innate immune activation enhances hiv acquisition in women, diminishing the effectiveness of tenofovir microbicide gel*. J Infect Dis, 2012. **206**(7): p. 993-1001.
44. Mansoor, L.E., et al., *Assessing the implementation effectiveness and safety of 1% tenofovir gel provision through family planning services in KwaZulu-Natal, South Africa: study protocol for an open-label randomized controlled trial*. Trials, 2014. **15**: p. 496.
45. Berger, R.E., *Re.: Effectiveness and safety of tenofovir gel, an antiretroviral microbicide, for the prevention of HIV infection in women*. J Urol, 2011. **185**(5): p. 1729.
46. Abdool Karim, Q., et al., *Effectiveness and safety of tenofovir gel, an antiretroviral microbicide, for the prevention of HIV infection in women*. Science, 2010. **329**(5996): p. 1168-74.
47. Gengiah, T.N., et al., *A drug evaluation of 1% tenofovir gel and tenofovir disoproxil fumarate tablets for the prevention of HIV infection*. Expert Opin Investig Drugs, 2012. **21**(5): p. 695-715.
48. Swaims-Kohlmeier, A., et al., *Proinflammatory oscillations over the menstrual cycle drives bystander CD4 T cell recruitment and SHIV susceptibility from vaginal challenge*. EBioMedicine, 2021. **69**: p. 103472.

49. Carias, A.M., et al., *Increases in Endogenous or Exogenous Progestins Promote Virus-Target Cell Interactions within the Non-human Primate Female Reproductive Tract*. PLoS Pathog, 2016. **12**(9): p. e1005885.
50. Swaims-Kohlmeier, A., et al., *Progesterone Levels Associate with a Novel Population of CCR5+CD38+ CD4 T Cells Resident in the Genital Mucosa with Lymphoid Trafficking Potential*. J Immunol, 2016. **197**(1): p. 368-76.
51. Passmore, J.A., H.B. Jaspan, and L. Masson, *Genital inflammation, immune activation and risk of sexual HIV acquisition*. Curr Opin HIV AIDS, 2016. **11**(2): p. 156-62.
52. Anderson, D.J., J. Marathe, and J. Pudney, *The structure of the human vaginal stratum corneum and its role in immune defense*. Am J Reprod Immunol, 2014. **71**(6): p. 618-23.
53. Chen, A., et al., *Modeling of Virion Collisions in Cervicovaginal Mucus Reveals Limits on Agglutination as the Protective Mechanism of Secretory Immunoglobulin A*. PLoS One, 2015. **10**(7): p. e0131351.
54. Lai, B.E.H., M. H.; Peters, J. J; Walmer, D. K.; Katz, D, *Transport Theory for HIV Diffusion through In Vivo Distributions of Topical Microbicide Gels*. Biophysical Journal, 2009. **97**.
55. Carias, A.M., et al., *Defining the interaction of HIV-1 with the mucosal barriers of the female reproductive tract*. J Virol, 2013. **87**(21): p. 11388-400.
56. Allen, S.A., et al., *Characterization of the Influence of Semen-Derived Enhancer of Virus Infection on the Interaction of HIV-1 with Female Reproductive Tract Tissues*. J Virol, 2015. **89**(10): p. 5569-80.
57. Sigal, A., et al., *Cell-to-cell spread of HIV permits ongoing replication despite antiretroviral therapy*. Nature, 2011. **477**(7362): p. 95-8.
58. Kim, J.T., et al., *Dendritic cells efficiently transmit HIV to T Cells in a tenofovir and raltegravir insensitive manner*. PLoS One, 2018. **13**(1): p. e0189945.
59. Koch, A.L., *The logarithm in biology. 1. Mechanisms generating the log-normal distribution exactly*. J Theor Biol, 1966. **12**(2): p. 276-90.
60. Koch, A.L., *The logarithm in biology. II. Distributions simulating the log-normal*. J Theor Biol, 1969. **23**(2): p. 251-68.

61. Limpert, E.S., W.; Abbt, M., *Log-normal distributions across the sciences: keys and clues*. Bioscience, 2001. **51**.
62. Semmelink, H.J., et al., *Histomorphometric study of the lower urogenital tract in pre- and post-menopausal women*. Cytometry, 1990. **11**(6): p. 700-7.
63. Gupta, P., et al., *High viral load in semen of human immunodeficiency virus type 1-infected men at all stages of disease and its reduction by therapy with protease and nonnucleoside reverse transcriptase inhibitors*. J Virol, 1997. **71**(8): p. 6271-5.
64. Hellstrom, W.J., et al., *Semen and sperm reference ranges for men 45 years of age and older*. J Androl, 2006. **27**(3): p. 421-8.
65. Shanmugasundaram, U., et al., *Phenotype and functionality of CD4+ and CD8+ T cells in the upper reproductive tract of healthy premenopausal women*. Am J Reprod Immunol, 2014. **71**(2): p. 95-108.
66. Battistini Garcia, S.A. and N. Guzman, *Acquired Immune Deficiency Syndrome CD4+ Count*, in *StatPearls*. 2023: Treasure Island (FL).
67. Tigner, A., S.A. Ibrahim, and I.V. Murray, *Histology, White Blood Cell*, in *StatPearls*. 2023: Treasure Island (FL).
68. Patton, D.L., et al., *Epithelial cell layer thickness and immune cell populations in the normal human vagina at different stages of the menstrual cycle*. Am J Obstet Gynecol, 2000. **183**(4): p. 967-73.
69. Weld, E.D., *Limits of Detection and Limits of Infection: Quantitative HIV Measurement in the Era of U = U*. J Appl Lab Med, 2021. **6**(1): p. 324-326.
70. Delaney, K.P., et al., *Time Until Emergence of HIV Test Reactivity Following Infection With HIV-1: Implications for Interpreting Test Results and Retesting After Exposure*. Clin Infect Dis, 2017. **64**(1): p. 53-59.
71. Patel, P., et al., *Estimating per-act HIV transmission risk: a systematic review*. AIDS, 2014. **28**(10): p. 1509-19.
72. Phillips, D.M., *The role of cell-to-cell transmission in HIV infection*. AIDS, 1994. **8**(6): p. 719-31.
73. Iwami, S., et al., *Cell-to-cell infection by HIV contributes over half of virus infection*. Elife, 2015. **4**.

74. Carr, J.M., et al., *Rapid and efficient cell-to-cell transmission of human immunodeficiency virus infection from monocyte-derived macrophages to peripheral blood lymphocytes*. *Virology*, 1999. **265**(2): p. 319-29.
75. Eschenbach, D.A., et al., *Influence of the normal menstrual cycle on vaginal tissue, discharge, and microflora*. *Clin Infect Dis*, 2000. **30**(6): p. 901-7.
76. Thiyagarajan, D.K., H. Basit, and R. Jeanmonod, *Physiology, Menstrual Cycle*, in *StatPearls*. 2023: Treasure Island (FL).
77. Kersh, E.N., et al., *SHIV susceptibility changes during the menstrual cycle of pigtail macaques*. *J Med Primatol*, 2014. **43**(5): p. 310-6.
78. Vassiliadou, N., L. Tucker, and D.J. Anderson, *Progesterone-induced inhibition of chemokine receptor expression on peripheral blood mononuclear cells correlates with reduced HIV-1 infectability in vitro*. *J Immunol*, 1999. **162**(12): p. 7510-8.
79. Vishwanathan, S.A., et al., *High susceptibility to repeated, low-dose, vaginal SHIV exposure late in the luteal phase of the menstrual cycle of pigtail macaques*. *J Acquir Immune Defic Syndr*, 2011. **57**(4): p. 261-4.
80. Nelson, P.W.M., J. D.; Perelson, A. S., *A model of HIV-1 pathogenesis that includes an intracellular delay*. *Math Biosci*, 2000. **163**.
81. Owen, D.H. and D.F. Katz, *A vaginal fluid simulant*. *Contraception*, 1999. **59**(2): p. 91-5.
82. Hladik, F. and M.J. McElrath, *Setting the stage: host invasion by HIV*. *Nat Rev Immunol*, 2008. **8**(6): p. 447-57.
83. Dimopoulos, Y., E. Moysi, and C. Petrovas, *The Lymph Node in HIV Pathogenesis*. *Curr HIV/AIDS Rep*, 2017. **14**(4): p. 133-140.
84. Lederman, M.M. and L. Margolis, *The lymph node in HIV pathogenesis*. *Semin Immunol*, 2008. **20**(3): p. 187-95.
85. Farmer, P., et al., *Expansion of cancer care and control in countries of low and middle income: a call to action*. *Lancet*, 2010. **376**(9747): p. 1186-93.
86. Orlando, A., et al., *Treatment of small hepatocellular carcinoma with percutaneous ethanol injection: a validated prognostic model*. *Am J Gastroenterol*, 2000. **95**(10): p. 2921-7.

87. Goldberg, E.P., et al., *Intratumoral cancer chemotherapy and immunotherapy: opportunities for nonsystemic preoperative drug delivery*. J Pharm Pharmacol, 2002. **54**(2): p. 159-80.
88. Sun, X., et al., *Intratumorally Injected Photothermal Agent-Loaded Photodynamic Nanocarriers for Ablation of Orthotopic Melanoma and Breast Cancer*. ACS Biomater Sci Eng, 2019. **5**(2): p. 724-739.
89. Hong, W.X., et al., *Intratumoral Immunotherapy for Early-stage Solid Tumors*. Clin Cancer Res, 2020. **26**(13): p. 3091-3099.
90. Willink, C.Y., et al., *Intratumoral injection therapies for locally advanced pancreatic cancer: systematic review*. BJS Open, 2023. **7**(3).
91. Marabelle, A., et al., *Starting the fight in the tumor: expert recommendations for the development of human intratumoral immunotherapy (HIT-IT)*. Ann Oncol, 2018. **29**(11): p. 2163-2174.
92. Chitkara, D., et al., *Biodegradable injectable in situ depot-forming drug delivery systems*. Macromol Biosci, 2006. **6**(12): p. 977-90.
93. McGuire, S., D. Zaharoff, and F. Yuan, *Nonlinear dependence of hydraulic conductivity on tissue deformation during intratumoral infusion*. Ann Biomed Eng, 2006. **34**(7): p. 1173-81.
94. Lee, D.H., J.; Leong, D.; Shin, J.; Yun, A.; Kim, J., *Physical, mathematical, and numerical derivations of the Cahn-Hilliard Equation*. Computational Materials Science, 2014. **81**.
95. Ham, S., et al., *An Explicit Adaptive Finite Difference Method for the Cahn-Hilliard Equation*. J Nonlinear Sci, 2022. **32**(6): p. 80.
96. Kim, J.S., L.; Choi, Y.; Lee, S.; Jeong, D *Basic Principles and Practical Applications of the Cahn Hilliard Equation*. Mathematical Problems in Engineering, 2016. **2016**.
97. Pratt, K.C.W., W. A., *The mutual diffusion coefficients of ethanol-water mixtures: determination by a rapid, new method*. Proceedings of the Royal Society of London Series a-Mathematical and Physical Sciences, 1974. **336**.
98. Hajjarian, Z., et al., *Mapping Mechanical Properties of the Tumor Microenvironment by Laser Speckle Rheological Microscopy*. Cancer Res, 2021. **81**(18): p. 4874-4885.

99. Ramiao, N.G., et al., *Biomechanical properties of breast tissue, a state-of-the-art review*. Biomech Model Mechanobiol, 2016. **15**(5): p. 1307-23.
100. Guimaraes, C.F.G., L.; Marques, A.P.; Reis, R.L., *The stiffness of living tissues and its implications for tissue engineering*. Nature Reviews Materials, 2020. **5**.
101. Mueller, S. and L. Sandrin, *Liver stiffness: a novel parameter for the diagnosis of liver disease*. Hepat Med, 2010. **2**: p. 49-67.
102. Myers, K.M., et al., *The mechanical role of the cervix in pregnancy*. J Biomech, 2015. **48**(9): p. 1511-23.
103. Baah-Dwomoh, A.M., J.; Tan, T.; De Vita, R., *Mechanical Properties of Female Reproductive Organs and Supporting Connective Tissues: A Review of the Current State of Knowledge*. Applied Mechanics Reviews, 2016. **68**(6).
104. Stylianopoulos, T., L.L. Munn, and R.K. Jain, *Reengineering the Physical Microenvironment of Tumors to Improve Drug Delivery and Efficacy: From Mathematical Modeling to Bench to Bedside*. Trends Cancer, 2018. **4**(4): p. 292-319.
105. Navindaran, K., J.S. Kang, and K. Moon, *Techniques for characterizing mechanical properties of soft tissues*. J Mech Behav Biomed Mater, 2023. **138**: p. 105575.
106. Oeda, S., et al., *Accuracy of liver stiffness measurement and controlled attenuation parameter using FibroScan((R)) M/XL probes to diagnose liver fibrosis and steatosis in patients with nonalcoholic fatty liver disease: a multicenter prospective study*. J Gastroenterol, 2020. **55**(4): p. 428-440.
107. McKnight, A.L., et al., *MR elastography of breast cancer: preliminary results*. AJR Am J Roentgenol, 2002. **178**(6): p. 1411-7.
108. Jiang, Y., et al., *Targeting extracellular matrix stiffness and mechanotransducers to improve cancer therapy*. J Hematol Oncol, 2022. **15**(1): p. 34.
109. Ansardamavandi, A., et al., *Quantification of effects of cancer on elastic properties of breast tissue by Atomic Force Microscopy*. J Mech Behav Biomed Mater, 2016. **60**: p. 234-242.
110. Jung, K.S., et al., *Risk assessment of hepatitis B virus-related hepatocellular carcinoma development using liver stiffness measurement (FibroScan)*. Hepatology, 2011. **53**(3): p. 885-94.

111. Hu, J., et al., *Diagnosis of liver tumors by multimodal ultrasound imaging*. *Medicine (Baltimore)*, 2020. **99**(32): p. e21652.
112. Wang, X.L., S. Lin, and G.R. Lyu, *Advances in the clinical application of ultrasound elastography in uterine imaging*. *Insights Imaging*, 2022. **13**(1): p. 141.
113. Salvati, H.P., P.; Debautt, C.; Ceelen, W., *Hydraulic conductivity of human cancer tissue: A hybrid study*. *Bioengineering & Translational Medicine*, 2023. **10617**.
114. Liu, L.J. and M. Schlesinger, *Interstitial hydraulic conductivity and interstitial fluid pressure for avascular or poorly vascularized tumors*. *J Theor Biol*, 2015. **380**: p. 1-8.
115. Liu, L.J., et al., *Estimation of Tumor Interstitial Fluid Pressure (TIFP) Noninvasively*. *PLoS One*, 2016. **11**(7): p. e0140892.
116. Milosevic, M., et al., *Interstitial permeability and elasticity in human cervix cancer*. *Microvasc Res*, 2008. **75**(3): p. 381-90.
117. Majumder, S., M.T. Islam, and R. Righetti, *Non-invasive imaging of interstitial fluid transport parameters in solid tumors in vivo*. *Sci Rep*, 2023. **13**(1): p. 7132.
118. Nief, C.A., et al., *Targeting Tumor Acidosis and Regulatory T Cells Unmasks Anti-Metastatic Potential of Local Tumor Ablation in Triple-Negative Breast Cancer*. *Int J Mol Sci*, 2022. **23**(15).
119. Lai, Y.E., et al., *Minimally invasive ethyl cellulose ethanol ablation in domesticated cats with naturally occurring head and neck cancers: Six cats*. *Vet Comp Oncol*, 2021. **19**(3): p. 492-500.
120. Robinson, J.A., et al., *Comparison of Dapivirine Vaginal Gel and Film Formulation Pharmacokinetics and Pharmacodynamics (FAME 02B)*. *AIDS Res Hum Retroviruses*, 2017. **33**(4): p. 339-346.
121. Chahine, E.B. and S.H. Durham, *Ibalizumab: The First Monoclonal Antibody for the Treatment of HIV-1 Infection*. *Ann Pharmacother*, 2021. **55**(2): p. 230-239.
122. Miner, M.D., L. Corey, and D. Montefiori, *Broadly neutralizing monoclonal antibodies for HIV prevention*. *J Int AIDS Soc*, 2021. **24 Suppl 7**(Suppl 7): p. e25829.
123. Dumiak, M., *Making it to manufacturing. The potential success of broadly neutralizing monoclonal antibodies for HIV prevention, treatment, and possibly even a cure could come at a cost*. *IAVI Rep*, 2014. **18**(2): p. 4-7, 17.